

# LOCATING THE EARTH'S MAGNETOPAUSE THROUGH X-RAY IMAGING

PANAGIOTA BOSKOU



Analysis of simulations in preparation for the SMILE mission

M2 IRT Space Science and Technology  
Observatoire de Paris

June 2025

Panagiota Boskou: *Locating the Earth's Magnetopause through X-ray imaging*,  
Analysis of simulations in preparation for the SMILE mission, © June 2025

**SUPERVISORS:**

Dr. Dimitra Koutroumpa  
Prof. Ronan Modolo

**LOCATION:**

Paris, France

**CONTEXT:**

Master Thesis, M2 IRT Space Science and Technology  
Observatoire de Paris, PSL

**HOSTING LABORATORY:**

Labratoire ATMosphères et Observations Spatiales (LATMOS)

## RÉSUMÉ

---

Malgré le développement de plusieurs modèles empiriques de la magnétopause basés sur des analyses statistiques des traversées *in situ*, la capture de la dynamique globale de la magnétopause reste un défi majeur. Ce travail présente de nouvelles avancées dans la modélisation de l'émission de rayons X produite dans la magnétogaine terrestre par les processus d'échange de charge du vent solaire (Solar Wind Charge eXchange, SWCX). Découverte et expliquée initialement dans le cas des comètes [3], cette émission, générée par des ions du vent solaire fortement chargés (par ex. O<sup>+7</sup>), a également été observée dans le gaz interplanétaire, autour des planètes, dans la magnétogaine terrestre, etc. [14]. L'émission SWCX dans la magnétogaine de la Terre constitue la cible de la future mission spatiale conjointe de l'ESA et de la CAS, appelée SMILE (Solar wind Magnetosphere Ionosphere Link Explorer). L'objectif de cette étude est de développer une méthodologie permettant d'explorer la dynamique globale de la magnétopause en exploitant les capacités d'observation à distance du télescope à rayons X mous (Soft X-ray Imager, SXI) embarqué à bord de la mission. Dans cette optique, l'équipe a développé le modèle LATMOS Test Particle (LaTeP), un modèle à particules test utilisant des champs électriques (E) et magnétiques (B) issus de simulations MHD ([OpenGGCM](#)), capable d'estimer les niveaux de flux de rayons X dans la magnétogaine terrestre. Dans le modèle LaTeP, des particules tests numériques représentant des ions O<sup>+7</sup> sont suivies, en résolvant leur équation de mouvement dans les champs E et B issus des simulations MHD, et la probabilité de leur échange de charge avec des atomes d'hydrogène de l'exosphère terrestre est calculée. Les cubes d'émission de rayons X produits sont projetés et intégrés sur le cône du champ de vision (Field of View, FOV) de l'instrument, fournissant des images synthétiques de SXI. Nous proposons une méthodologie pour retrouver la position instantanée et la topologie de la magnétopause à partir d'images uniques de SXI. Cette approche repose sur l'hypothèse selon laquelle la direction tangente à la magnétopause coïncide avec la courbe d'intensité maximale dans l'image [15], hypothèse que nous testons par rapport aux données d'entrée des simulations. Une chaîne de traitement a été développée pour ajuster les courbes tangentes des modèles empiriques aux courbes d'émission maximale dérivées des images, et les performances sont évaluées à la fois par rapport aux maxima d'intensité et à la magnétopause extraite des simulations. En supposant un modèle empirique donné, cette technique permet de retrouver les paramètres optimaux du modèle et de fournir une évaluation quantitative de sa performance. À partir des paramètres ajustés, on peut reconstruire la surface, donnant des informations sur la position et la forme de la magnétopause.<sup>1</sup>

---

<sup>1</sup> Automatically translated abstract, using generative artificial intelligence.

## ABSTRACT

---

Despite the development of several empirical magnetopause models based on statistical analyses of in-situ crossings, capturing the global dynamics of the magnetopause remains a significant challenge. Current work discusses new steps in the modeling of the X-ray emission produced in the Earth's magnetosheath due to the Solar Wind Charge eXchange (SWCX) processes. Initially discovered and explained for comets [3], this emission, produced by highly charged solar wind ions (e.g. O<sup>7+</sup>), has also been observed from interplanetary gas, planets, terrestrial magnetosheath, etc.[14]. SWCX emission in the Earth's magnetosheath will be the target of the future joint European Space Agency (ESA) and Chinese Academy of Sciences (CAS) space mission called SMILE (Solar wind Magnetosphere Ionosphere Link Explorer). The goal of the current study is to develop a methodology that will probe the global dynamics of the magnetopause, by utilizing the remote sensing capabilities of the Soft X-ray Imager (SXI) onboard. In this light, the team has developed the LATMOS Test Particle (LaTeP) model, a Test Particle (TP) model with input electric (E) and magnetic (B) fields from MHD ([OpenG-GCM](#)) simulations, that is capable of estimating the levels of X-ray flux in the Earth's magnetosheath. In the LaTeP model, we follow numerical test-particles, representing O<sup>7+</sup> ions, solving their motion equation as they propagate in the MHD-computed E and B fields, and calculate the probability of them charge exchanging with hydrogen atoms from the Earth's exosphere. The produced X-ray emission cubes are being projected and integrated over the imager's Field of View (FOV) cone, returning the synthetic images of the SXI instrument. We propose a methodology for retrieving the instantaneous location and topology of the magnetopause from single SXI images. This approach assumes that the magnetopause's tangent direction coincides with the curve of maximum intensity in the image [15], a hypothesis we test against simulation inputs. A processing pipeline is developed to fit the empirical model tangent curves to the image-derived maximum emission curves, and performance is benchmarked both against the intensity maxima and the simulation-extracted magnetopause. Assuming a given empirical model, this technique enables the retrieval of optimal model parameters and provides a quantitative assessment of model performance. From the fitted parameters we can reconstruct the surface, providing information about the location and shape of the magnetopause.

## ACKNOWLEDGMENTS

---

I am truly grateful to my supervisors, Dimitra Koutroumpa and Ronan Modolo, for their constant support throughout the development of this work, as well as for their immense help in my academic growth. They have provided me with invaluable tools and lessons that I will proudly carry forward in my academic career. I shall do my best to put them to good use. I would also like to thank the Observatoire de Paris and Campus France for their support throughout the master. This work would not have been possible without them.

## CONTENTS

---

1	INTRODUCTION	1
1.1	Earth's Space Environment	1
1.2	Earth's Magnetopause	2
1.3	Detecting the magnetopause	4
1.3.1	In-situ satellite measurements	4
1.3.2	Imaging the magnetopause	7
1.4	Previous work: Fitting methods	10
2	THE TANGENT HYPOTHESIS	13
2.1	Extracting the magnetopause surface from the simulation	13
2.1.1	LaTeP model: Emissivity cube	13
2.1.2	Shue model fitted to slices	15
2.1.3	Radial extraction of full magnetopause	16
2.1.4	Fitting models to surface	20
2.1.5	Extracting the magnetopause from the MHD emissivity	22
2.2	Extracting the maximum intensity curve from the image	24
2.2.1	Constructing the images	25
2.2.2	Image processing	26
2.3	Characterizing the tangent hypothesis	28
2.3.1	Projecting the surface	28
2.3.2	Results: Characterizing the Tangent Hypothesis	30
3	TANGENT FITTING	35
3.1	The method	36
3.2	Benchmarking the fitting method	38
3.2.1	Image-fitted Shue to cube-fitted Shue	38
3.2.2	Characterization through maximum intensity curve	40
3.2.3	Discussion and Future developments	42
A	PERFORMANCE OVER MULTIPLE ORBITS	44
A.1	Tangent Hypothesis	44
A.2	Tangent Fitting	47
	BIBLIOGRAPHY	48

## LIST OF FIGURES

---

Figure 1	Earth's space environment	2
Figure 2	Magnetopause and current sheet topology [1].	4
Figure 3	Magnetopause crossings.	5
Figure 4	GSE and spherical coordinates.	5
Figure 5	The SMILE orbit. SXI and UVI Field of View and key regions, credit: ESA	9
Figure 6	Magnetopause extraction techniques and their assumptions/required input [19].	11
Figure 7	Integration of emissivity for observers at infinity along the Z and Y-axis.	14
Figure 8	Integration over z.	15
Figure 9	Zero-contour lines and the corresponding fitted Shue model	16
Figure 10	Emissivity cube slices in spherical coordinates.	17
Figure 11	Emissivity over radius for different $\theta$ directions in the $\text{phi} = 90^\circ$ plane	17
Figure 12	Extraction of maximum emissivity surface from the LaTeP cube.	18
Figure 13	Extraction of emissivity peaks below an emissivity threshold surface from the LaTeP cube.	19
Figure 14	Extraction of emissivity peaks below an emissivity and above a radius threshold surface from the LaTeP cube.	19
Figure 15	Shue and Lin model fitted to the maximum emissivity surface extracted from LaTeP.	21
Figure 16	Liu model fitted to the maximum emissivity surface extracted from LaTeP.	21
Figure 17	MHD emissivity cube slices in spherical coordinates.	22
Figure 18	MHD emissivity over radius for different $\theta$ directions in the $\text{phi} = 90^\circ$ plane	23
Figure 19	3D surfaces extracted from MHD emissivity cube.	23
Figure 20	MHD emissivity over radius for different $\theta$ directions in the $\text{phi} = 90^\circ$ plane	24
Figure 21	Final magnetopause surface. First and Second maxima peaks of MHD emissivity cubes.	25
Figure 22	3D View CDPP software	25
Figure 23	Typical behavior of SXI images.	26
Figure 24	Polynomials fitted to noisy maximum intensity arc.	27
Figure 25	Arc detection after different filters and imaging processing techniques have been applied.	27

Figure 26	Extraction of tangent point to satellite for a numerical surface. <a href="#">28</a>
Figure 27	Evolution of RMSE over time elapsed from 2 June 2025 00:00 UTC and key snapshots. Magnetopause projection is indicated in blue while the red curve indicates the detected maximum intensity arc. <a href="#">30</a>
Figure 28	Evolution of RMSE over time elapsed from 1st November 2025 00:00 UTC and key snapshots. <a href="#">31</a>
Figure 29	Evolution of RMSE over time elapsed from 1st April 2026 00:00 UTC and key snapshots. <a href="#">32</a>
Figure 30	Viewing direction correlated with surface projection and image processing problems <a href="#">33</a>
Figure 31	Orbit precession and corresponding viewing angles for June, November and April. <a href="#">33</a>
Figure 32	Orbital dependency of RMSE over a year. <a href="#">34</a>
Figure 33	Input image constructed from MHD simulations and output image of the SXI noise and background simulator. [16] <a href="#">35</a>
Figure 34	Projecting the tangent points of Shue surfaces. <a href="#">38</a>
Figure 35	Parameter and Image space of Hough transform. <a href="#">38</a>
Figure 36	Evolution of $r_0$ over time elapsed from 1st August 2025 09:00 UTC and key snapshots. <a href="#">39</a>
Figure 37	Cube-fitted Shue model to Image-fitted model RMSE in degrees and RE. <a href="#">40</a>
Figure 38	Deviation of image-fitted parameters from initial cube-fitted parameters $r_0$ and $\alpha$ . <a href="#">41</a>
Figure 39	Evolution of fitted Shue curves to maximum intensity arcs RMSE over time elapsed from 1st August 2025 09:00 UTC. <a href="#">41</a>
Figure 40	Full orbit images for June 2025. <a href="#">44</a>
Figure 41	Full orbit images for November 2025. <a href="#">45</a>
Figure 42	Full orbit images for April 2026. <a href="#">46</a>
Figure 43	Full orbit images for August 2025. <a href="#">47</a>

## LIST OF TABLES

---

Table 1	Initial OpenGGCM simulation parameters. <a href="#">15</a>
Table 2	Shue model parameters, fitted to LaTeP maximum emissivity surface. <a href="#">20</a>
Table 3	Lin model parameters, fitted to LaTeP maximum emissivity surface. <a href="#">21</a>
Table 4	Liu model parameters, fitted to LaTeP maximum emissivity surface. <a href="#">22</a>

## ACRONYMS

---

FOV	Field Of View
LaTeP	Latmos Test Particle
IMF	Interplanetary Magnetic Field
NetCDF	Network Common Data Form
GSE	Geocentric Solar Ecliptic
GSM	Geocentric Solar Magnetospheric
RE	Earth Radii
POV	Point Of View
MHD	MagnetoHydroDynamics
SW	Solar Wind
SXI	Soft X-ray Imager
LOS	Line Of Sight
RMSE	Root Mean Square
TFA	Tangent Fitting Approach
BFA	Boundary Fitting Approach
TDA	Tangential Direction Approach
SMILE	Solar wind Magnetosphere Ionosphere Link Explorer
ESA	European Space Agency
CAS	Chinese Academy of Sciences
SWCX	Solar Wind Charge eXchange
RE	Earth Radii
UVI	UltraViolet Imager
MAG	Magnetometer
LIA	Light Ion Analyser

## INTRODUCTION

---

Although the matter we encounter daily on Earth's surface predominantly exists in solid, liquid, or gaseous states, the vast majority of baryonic matter in the universe exists in a fourth state: plasma. This state of matter displays complex behaviors that have not been completely understood due to the lack of proximity to naturally occurring plasmas as well as their vast diversity in density and temperature. The closest natural laboratory to study these plasmas is the Earth itself, particularly in the region above approximately 100 km altitude, where the phenomena that take place are dominated by electromagnetic interactions and should be treated using plasma physical methods. A key point of interest is the interaction and coupling of the Sun - Earth system, also known as space weather. We will attempt to study this connection and the physics between the interaction of the Sun's emitted particles and the terrestrial space environment.

### 1.1 EARTH'S SPACE ENVIRONMENT

We characterize this region as the Earth's space environment, consisting of the magnetosphere and its neighboring plasma regions, that display strong coupling, as well as a plethora of different phenomena. To understand this environment we shall start from its driving forces:

The Sun emits magnetized supersonic plasma with typical speeds of 300 to 800 km/s. This is known as the Solar Wind ([SW](#)), consisting mainly of electrons, protons and alpha particles, as well as traces of atomic nuclei and heavy ions found in the solar corona, such as carbon, nitrogen, oxygen, neon, magnesium, silicon, sulfur, and iron. The solar wind plasma is highly conductive meaning the magnetic field lines and the plasma flows are "frozen" together and the coronal magnetic field is dragged out by the solar wind to form the Interplanetary Magnetic Field ([IMF](#)).

This takes the shape of an Archimedean spiral pattern due the combination of the outward motion of the solar wind and the Sun's rotation, known as the Parker spiral [[12](#)] and shown schematically in [Figure 1a](#). Near the Earth, the [IMF](#) can be expressed as a three-dimensional vector  $\vec{B} = B_x \vec{x} + B_y \vec{y} + B_z \vec{z}$ . Its coupling to the Earth's magnetic field is correlated with its local orientation. We can parametrize this through the 'clock angle'  $\Omega$ , which describes the orientation of the magnetic field in the Y-Z plane of the Geocentric Solar Magnetospheric ([GSM](#)) coordinate system. A clock angle of  $0^\circ$  means the [IMF](#) points northward, parallel to Earth's magnetic dipole, while a clock angle of  $180^\circ$  means the [IMF](#) points southward.

The Earth generates its own magnetic field as well, owing its existence to the currents induced by the convective motion in its core. Due to its super-

sonic velocity, when the solar wind encounters an obstacle, like the Earth's magnetic field, it is decelerated and deflected, forming a bow shock where the kinetic energy of the supersonic plasma is partially converted to thermal energy. Shocks are discontinuities that are characterized by non-vanishing normal fluxes  $nv_n \neq 0$ , meaning the solar wind plasma can penetrate further towards the Earth. The region downstream of the bow shock, called the magnetosheath, contains this thermalized and dense plasma with a stronger magnetic field compared to the undisturbed solar wind. [1]

The frozen-in interplanetary magnetic field lines prevent penetration of the solar wind into the magnetosphere, the region where the magnetic field lines of the Earth dominate. The boundary separating these regions is the magnetopause, enclosing the magnetosphere—the cavity formed by the terrestrial magnetic field, compressed on the day-side and elongated into a magnetotail on the night-side by solar wind pressure.

*Discontinuities are sudden transition layers from one equilibrium state of the plasma to another. These boundaries abide to conservation laws resulting to different classes of discontinuities with corresponding jump conditions.*

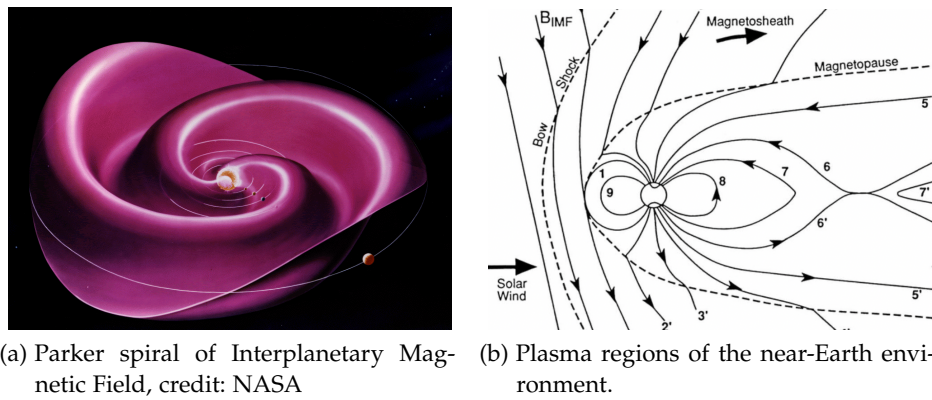


Figure 1: Earth's space environment

## 1.2 EARTH'S MAGNETOPAUSE

For a more precise definition of the magnetopause we shall first take a look at the properties of plasma discontinuities. Discontinuities separate plasma regions with distinct physical properties, which may change abruptly across the boundary. These changes are not arbitrary; the fields and plasma parameters must satisfy specific conditions derived from the conservation laws of mass, momentum, and energy. A standard approach to determine these boundary conditions is to integrate the MHD conservation equations across the discontinuity. This yields the Rankine-Hugoniot jump conditions, which relate quantities on both sides of the boundary.

Among the results, it follows that the normal component of the magnetic field is continuous across any discontinuity, and that the normal mass flux remains constant. Depending on how the remaining field and plasma components behave, three main classes of MHD discontinuities can be identified: tangential, rotational, and shock discontinuities. The magnetopause is most often treated as a tangential discontinuity, characterized by a discontinuous

change in the tangential magnetic field and plasma flow, but continuous normal components. There is no mass or magnetic flux transfer across the boundary, and the Rankine-Hugoniot jump conditions simplify to:

$$[v_n] = 0 \quad (\text{zero normal flow}) \quad (1)$$

$$[B_n] = 0 \quad (\text{zero normal magnetic field}) \quad (2)$$

$$[\rho v_n] = 0 \quad (\text{mass flux continuity}) \quad (3)$$

$$\left[ p + \frac{B^2}{2\mu_0} \right] = 0 \quad (\text{continuity of the total pressure}) \quad (4)$$

$$[\rho] \neq 0 \quad (\text{density can change}) \quad (5)$$

$$[v_t] \neq 0 \quad (\text{tangential velocity can change}) \quad (6)$$

$$[B_t] \neq 0 \quad (\text{tangential magnetic field can change}) \quad (7)$$

We can visualize these jumps, through the typical changes in plasma moments across a tangential discontinuity, in [Figure 3a](#). The continuity of the total pressure across the discontinuity defines a surface of total pressure balance between the two contacting plasmas with no mass or magnetic flux crossing the discontinuity from either side, while all other quantities can experience arbitrary changes. This implies, that as a tangential discontinuity the magnetopause is a surface of total pressure equilibrium between the solar wind magnetosheath plasma and the geomagnetic field confined in the magnetosphere. The IMF is quite weak near the Earth and the magnetopsheric plasma thermal and dynamic pressures can be neglected compared with the pressure of the geomagnetic field. We can therefore, request pressure equilibrium between the dynamic pressure of the solar wind and magnetic pressure of the magnetosphere, as a first approximation.

$$2\mu_0\kappa n_{sw}m_i \left( \frac{\nabla S_{mp}}{|\nabla S_{mp}|} \cdot \mathbf{v}_{sw} \right)^2 = \left( \frac{\nabla S_{mp}}{|\nabla S_{mp}|} \times \mathbf{B} \right)^2 \quad (8)$$

[Equation 8](#) contains the complicated structure of the magnetospheric magnetic field, as well as the three-dimensional derivatives of the unknown magnetopause surface  $S_{mp}$ . It is a second-order three-dimensional nonlinear partial differential equation, and is therefore solvable only with numerical methods. Solving for the surface in the meridional plane, we get no continuous solution connecting the dayside magnetopause to the nightside magnetopause, while in the equatorial plane the magnetopause is a smooth curve extending from the dayside into an open tail. This point of discontinuity is defined as the polar cusp. A schematic of this solution can be found in [Figure 2a](#).

The ions and electrons that are reflected at the boundary, perform partial gyro-orbits within the magnetospheric field. Their opposite gyration directions generate a net current localized near the magnetopause, with a thickness on the order of the ion gyroradius. This diamagnetic current enhances the internal magnetic field and cancels the external one, maintaining pressure balance across the boundary. We refer to this as the magnetopause current sheet, and a schematic of its structure is shown in [Figure 2b](#). [1]

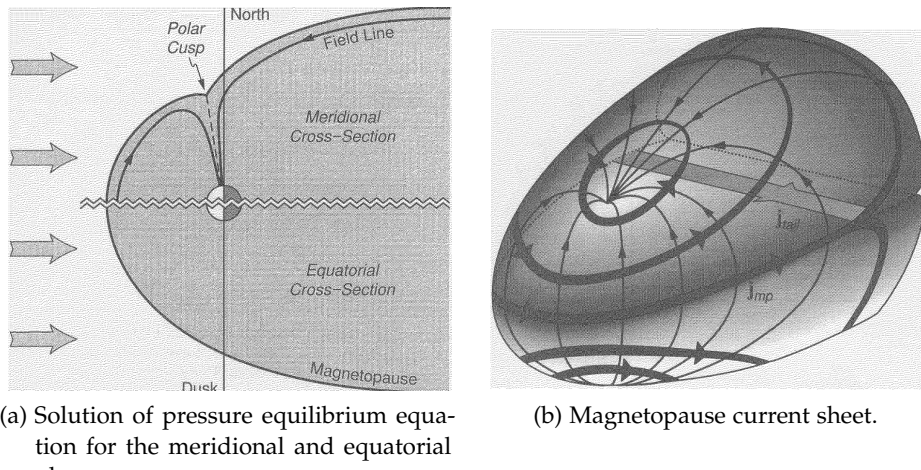


Figure 2: Magnetopause and current sheet topology [1].

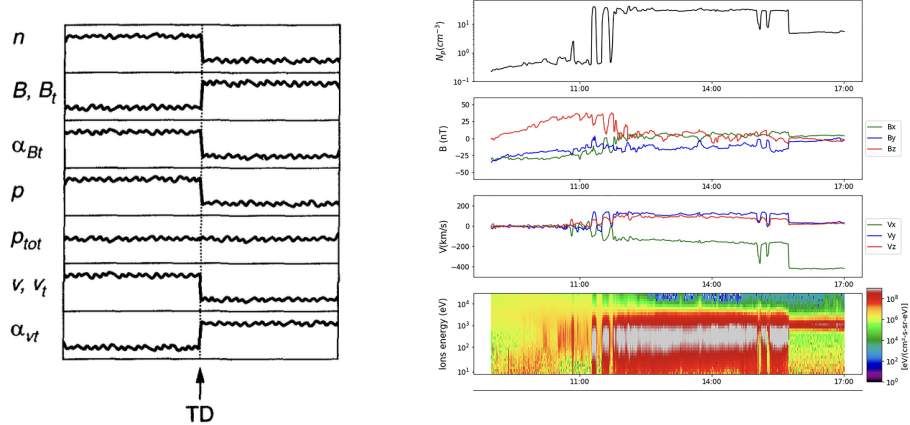
### 1.3 DETECTING THE MAGNETOPAUSE

Understanding the shape and location of the magnetopause is crucial to explaining the dynamics and processes of geophysical plasmas, and particularly the response of the magnetosphere to the solar wind. How does the subsolar point change with the dynamic and magnetic pressure of the solar wind? How does the IMF affect the position of the cusps, and what can this indicate for the magnetic reconnection that takes place to form them? With which processes can this collisionless plasma interact with obstacles and display fluid like behavior?

#### 1.3.1 *In-situ satellite measurements*

We have partial answers to these questions through in-situ measurements of satellite crossings. By analyzing the measurements of instruments on board and detecting abrupt changes in parameters such as density, temperature, flow velocity, and magnetic field orientation, we can identify the location and type of discontinuity and correlate it with the position of the satellite. A typical magnetopause crossing from the Cluster 1 spacecraft is shown in Figure 3b.

In order to derive information about the global behavior of this surface, one must compile a catalog of boundary crossings from multiple in situ data of such missions. This quite a time-consuming task, as well as ambiguous concerning the interpretation of the measurements and the precise definition and automatic detection of the crossings. The ever-growing amount of data collected by the satellites, therefore does not linearly translate to increasing number of catalogs [10]. Additionally, the dynamic nature of the response of the magnetopause to the solar wind, make the correlation of local measurements, with the global shape and dynamics of the magnetopause challenging. Nonetheless, various studies have attempted characterizing and



(a) Typical behavior of plasma moments along a tangential discontinuity [1].

(b) Cluster 1 spacecraft measurements while crossing from the solar wind to the magnetosheath to the magnetosphere [10].

Figure 3: Magnetopause crossings.

parametrizing this shape with [SW](#) and magnetospheric parameters, building thus empirical models of the surface.

#### 1.3.1.1 Coordinate system

Before moving any further, we shall define our main coordinate systems and frames, for consistency. The most common frame we will be using is the Geocentric Solar Ecliptic ([GSE](#)) system. This has its X-axis pointing from the Earth toward the Sun and its Y-axis is chosen to be in the ecliptic plane pointing towards dusk (thus opposing planetary motion). Its Z-axis is parallel to the ecliptic pole. Relative to an inertial system this system has a yearly rotation.

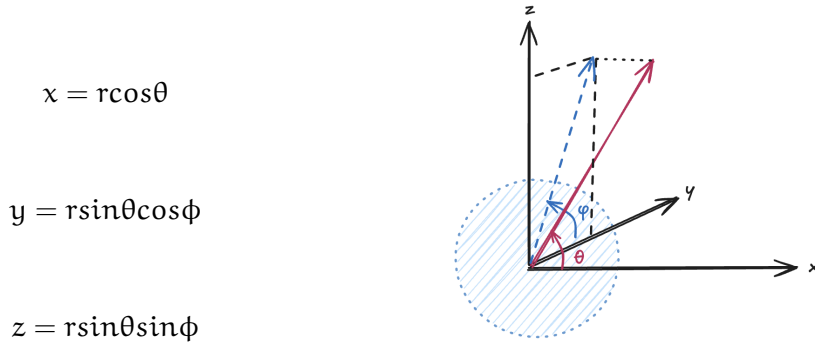


Figure 4: GSE and spherical coordinates.

We can define a spherical system based on the cartesian [GSE](#), that will help us describe the magnetopause as a parametrized radial function of the spherical angles  $r(\theta, \phi)$ . We follow the convention of previous papers [19], where  $\theta$  is the angle between  $\vec{r}$  and the X-axis, and  $\phi$  is the angle between the

Y-axis and the projection of  $\vec{r}$  to the YZ plane. The coordinate transformation from spherical to GSE is therefore defined as in [Figure 4](#).

### 1.3.1.2 Empirical models

Moving back to the study of the magnetopause surface through the statistical analysis of crossings, we will look into the main empirical models that have been proposed. The first and simplest empirical model was proposed by Shue et al. and is described by [Equation 9](#).

$$r(\theta) = r_0 \left( \frac{2}{1 + \cos \theta} \right)^\alpha \quad (9)$$

where:

- $r(\theta)$  Radial distance of the magnetopause from the Earth's center at a given polar angle  $\theta$
- $R_E$  Earth's radius (6371 km)
- $\alpha$  the flaring parameter, given by:  

$$\alpha = (0.58 - 0.01B_z)(1 + 0.01P_{dyn})$$
- $P_{dyn}$  Dynamic pressure of the solar wind (in nPa)  

$$P_{dyn} = 1.15 \cdot n \cdot v_x^2 \cdot 1.67 \times 10^{-6}$$
- $r_0$  Subsolar standoff distance of the magnetopause, given by:

$$r_0 = (11.4 + 0.013B_z)P_{dyn}^{-\frac{1}{6.6}}, \quad \text{for } B_z \geq 0$$

$$r_0 = (11.4 + 0.14B_z)P_{dyn}^{-\frac{1}{6.6}}, \quad \text{for } B_z < 0$$

Here, the relations that are given for  $\alpha$  and  $r_0$  are the parametrization with respect to the solar wind and magnetospheric parameters, derived in the original paper [17]. The crossings used to construct this model were taken from satellites of equatorial orbit, and thus assumes a rotational symmetry over the X-axis. As expected from the numerical solution of the surface in the equatorial plane, no discontinuity arises, and therefore the Shue model describes a smooth surface with no indentations.

Later evidence of dipole tilt, indentation in the near-cusp region, and dawn-dusk asymmetry led to the development of more refined models. One such improvement was introduced by Lin et al., who proposed an empirical magnetopause model that included an azimuthal asymmetry induced by the dipole tilt angle and also kept the possibility of a dawn-dusk asymmetry [7]. In his paper Liu et al. combined THEMIS data and MHD simulations to derive a more sophisticated geometry and parametrization [9]. We will describe these models concisely, as expressed by Nguyen et al. [11], where he defines the general form [Equation 10](#).

$$r = r_0 \left( \frac{2}{1 + \cos \theta} \right)^\xi + Q \quad (10)$$

where,  $Q$  is an additive term that defines the geometry of the cusps, and is different for the two models. For the Lin model, this term is expressed by:

$$\begin{aligned}
Q &= C \left( e^{d_n \psi_n^{4/5}} + e^{d_s \psi_s^{4/5}} \right) \\
C &= a_9 (P_{dyn} + P_n)^{a_{10}} \\
d_{n,s} &= a_{11} \pm a_{12} \gamma + a_{13} \gamma^2 \\
\psi_n &= \arccos(\cos(\theta) \cos(\theta_n) + \sin(\theta) \sin(\theta_n) \cos(\phi)) \\
\psi_s &= \arccos(\cos(\theta) \cos(\theta_s) + \sin(\theta) \sin(\theta_s) \cos(\phi - \pi)) \\
\theta_{n,s} &= a_{14} \pm a_{15} \gamma
\end{aligned}$$

The terms  $\psi_n$  and  $\psi_s$  describe the angular distance from the cusp indentations in the northern and southern hemispheres, respectively. The additive term of the Liu model is described by the following equations:

$$\begin{aligned}
Q &= -a_9 C r_0 \left( \frac{2}{1 + \cos \theta} \right)^\xi \cos^2 \phi \\
C &= e^{-|\theta - l_n|/w} (1 + \text{sgn}(\cos \phi)) + e^{-|\theta - l_s|/w} (1 + \text{sgn}(\cos(-\phi))) \\
l_{n,s} &= (a_{10} + a_{11} \tanh[a_{12}(B_z + a_{13})]) (1 \mp a_{14} \gamma) \\
w &= (a_{15} + a_{16} \log(P_{dyn})) (1 + a_{17} \gamma^2)
\end{aligned}$$

We advise the reader to refer to the corresponding studies for more information on the coefficients  $a_i$  and the way they are determined[11]. In his paper series, Nguyen et al., re-parametrizes and evaluates this models by analyzing multi-mission data and constructing a representative catalog. Among the many relevant results, is that the Lin model overestimates the indentation of the cusps, while the Liu model seems to be the best description of the selected crossings. We will see later on, that this comes in disagreement with some of our results, depending on how we define the magnetopause, and extra care must be taken to ensure consistent definitions.

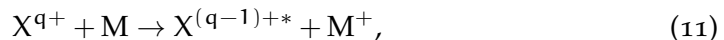
### 1.3.2 Imaging the magnetopause

It is evident that we have gained valuable knowledge from these in-situ measurements, however the global dynamics of the magnetopause and its response to the solar wind are still difficult to extract. The capability of remote sensing, or imaging of this boundary, would allow for more dynamic measurements; something that is crucial for understanding the coupling with the solar wind, which can be highly variable in a timescale of minutes. Under this scope, it was proposed that we could utilize the charge exchange phenomenon between the solar wind and the exosphere of the Earth, to achieve this new method of observation.

#### 1.3.2.1 Charge exchange

During its close approach to Earth, extreme ultraviolet and X-ray emission was observed from the comet C/Hyakutake 1996 B2 by the Röntgen X-ray

Satellite and Rossi X-ray Timing Explorer[8]. This emission was later interpreted by Cravens and the charge exchange emission mechanism was proposed. Under this mechanism, the multiply charged heavy ions of the solar wind can charge transfer with cometary neutrals, producing ions which can be highly excited and consequently emit photons in the extreme ultraviolet and x-ray part of the spectrum [3]. It was later suggested, that the same phenomenon could take place between the solar wind and the geocoronal hydrogen, leading to the terrestrial magnetosheath being luminous in the X-ray regime [14]. The emission in this case, is generated by charge exchange reactions between multiply charged heavy solar wind ions ( $O^{7+}, C^{5+}, \dots$ ) and the neutral particles (mostly hydrogen atoms) in the geocorona. The general Solar Wind Charge eXchange ([SWCX](#)) interaction is given by [Equation 11](#).



where the heavy and multiply charged ( $q+$ ) solar wind ion is noted as  $X^{q+}$  and the neutral particle is noted as  $M$ . Electrons are transferred from neutral particles to a high energy state of ions, imposing these ions into an excited state. When the excited ions de-excite to the lower-energy state, they emit photons in the soft X-ray band ( $E \leq 2\text{keV}$ ) [21]:



In their paper, Robertson and Cravens, simulated this emission as images, opening the discussion about remote sensing of the magnetosheath. Soft X-ray emissivity is expected to be strong in the dayside magnetosheath and cusp regions, where both solar wind ion and neutral particle densities are high. In contrast, the low density of solar wind ions within the magnetosphere and the scarcity of neutral hydrogen in the solar wind result in weak emission in those regions. As a result, a boundary in soft X-ray emission is expected at the magnetopause. This sharp increase in emission can be used to determine the magnetopause location through global soft X-ray imaging from space-based instruments. [18]

### 1.3.2.2 SMILE mission

The Solar wind Magnetosphere Ionosphere Link Explorer ([SMILE](#)) mission was proposed, in collaboration of [ESA](#) and [CAS](#), as an attempt in capturing this [SWCX](#) phenomenon in the Earth's magnetosheath. The satellite will be launched in 2026 into a highly elliptical polar orbit, with an apogee of  $\approx 20$  Earth Radii ([RE](#)), a perigee of  $\approx 1$  [RE](#), and an inclination of  $73^\circ$ . The orbital period is  $\approx 50.3$  hours, and a schematic of its orbit is shown in [Figure 5](#). The science payload on-board [SMILE](#) consists of the UltraViolet Imager ([UVI](#)), the Magnetometer ([MAG](#)), the Light Ion Analyser ([LIA](#)) and finally the Soft X-ray Imager ([SXI](#)). [SXI](#) is a wide Field Of View ([FOV](#)) X-ray telescope of  $15.5^\circ \times 26.5^\circ$ , designed to capture the emission of the magnetosheath, allowing the study of the magnetopause dynamics and its detection with a requirement of 0.5 [RE](#) accuracy. [16]

*The geocorona is the outermost region of the Earth's atmosphere, the exosphere, where collisions between particles are considered negligible. The density in this region is generally assumed to drop as*

$$n_H = 25 \left(\frac{10RE}{R}\right)^3 [\text{cm}^{-3}]$$

The preparation for space observations that haven't been performed before is no trivial task. Space missions require meticulous planning and therefore accurate predictions of the expected science data, as well as methods to optimize their return. The deployment of sophisticated simulations is therefore crucial prior to mission launch, both to facilitate operation planning and to develop pipelines for the analysis of the upcoming data. In this light, the [SMILE Modeling Working Group](#) was formed, in order to produce a simulation catalog for different [SW](#) conditions, with common input parameters.

The group aims to predict and interpret the images the [SXI](#) will generate, simulate the changes of magnetospheric boundary locations under different solar wind conditions, and extract magnetospheric boundary and cusp positions. To achieve these goals, the Modeling Working Group primarily relies on MagnetoHydroDynamics ([MHD](#)) simulations, which treat the plasma as a single fluid and are computationally efficient. [MHD](#) is well-suited for capturing large-scale dynamics and global structures - even in highly dynamic cases, but it lacks kinetic resolution and cannot distinguish between different ion species. As a result, [MHD](#)-based X-ray simulations tend to produce smooth, continuous images where the X-ray intensity is strictly proportional to the total proton flux. This leads to two key limitations: the inability to resolve spectroscopic features linked to specific ions, and the artificial production of X-rays within the magnetosphere due to the absence of a distinction between solar wind and magnetospheric plasma. The latter requires the introduction of an artificial mask inside the magnetosphere.

To address these issues, the LATMOS team developed the Latmos Test Particle ([LaTeP](#)) model, a test-particle model that simulates heavy ions kinetically. This intermediate approach introduces ion-specific behavior such as gyroradius effects and charge-exchange cross-section differences, enabling more realistic X-ray spectroscopic predictions and avoiding emission inside the magnetosphere. Since [LaTeP](#) does not compute E/B fields self-consistently, it relies on external electromagnetic field inputs provided by MHD codes such as [OpenGGCM](#), justified by the negligible feedback of highly charged ions due to their very low abundance ( $10^{-4}$  the proton density) in the solar wind. Through this approach, we can get the X-ray emissivity by following numerical test-particles, representing heavy ions. In this work we will focus on  $O^{7+}$  ions, since they are the most important contributors in the spectral energy range of the [SXI](#) detectors. Solving their equation of motion as they

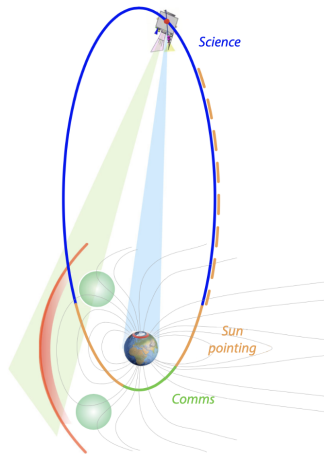


Figure 5: The SMILE orbit. SXI and UVI Field of View and key regions, credit: ESA

propagate in the MHD-computed E and B fields, we calculate the probability of them charge exchanging with hydrogen atoms from the Earth's exosphere. From this quantity, we can calculate the volume emissivity of X-ray Q in  $\text{eV cm}^{-3} \text{ s}^{-1}$ , as in [Equation 13](#). [21]

$$Q = n_M \cdot n_{X^{q+}} \cdot v_{X^{q+}} \cdot \sigma_{X^{q+}, M} \cdot Y_{X^{(q-1)+}} \quad (13)$$

where:

$Q$	Volume emissivity of soft X-rays (in $\text{eV cm}^{-3} \text{ s}^{-1}$ )
$n_M$	Neutral particle density ( $\text{cm}^{-3}$ )
$n_{X^{q+}}$	Density of solar wind ions with charge $q+$ ( $\text{cm}^{-3}$ )
$v_{X^{q+}}$	Plasma (ion) velocity ( $\text{cm s}^{-1}$ )
$\sigma_{X^{q+}, M}$	Cross-section for charge exchange between $X^{q+}$ and M ( $\text{cm}^2$ )
$Y_{X^{(q-1)+}}$	Energy of emitted line weighted by its emission probability (eV)

We can integrate this emissivity along a specific Line Of Sight (LOS) to obtain the intensity of each looking direction in  $\text{eV cm}^{-2} \text{ s}^{-1} \text{ sr}^{-1}$ . We also assume isotropic emission and divide by  $4\pi$  to get the emissivity in a particular direction.

$$I = \frac{1}{4\pi} \int_{\text{LOS}} Q \, ds \quad (14)$$

Calculating this quantity for each pixel's LOS of the imager, we can construct a synthetic image of the expected SXI data. This does not take into account the contribution from background sources nor the response of the instrument.

#### 1.4 PREVIOUS WORK: FITTING METHODS

When attempting to extract three-dimensional information from a two-dimensional image, one must make a set of assumptions to account for this loss of information. In this end, three notable techniques have been proposed to reconstruct the magnetopause using soft X-ray imaging.

The first is the Boundary Fitting Approach (BFA), introduced by Jorgensen et al. [6]. This method assumes parametrized forms for the magnetopause, and corresponding X-ray emissivity distribution based on MHD simulations. They then vary the parameters and generate a set of simulated images. These images are compared and fitted to the synthetic observed image, and the best-fit parameters define the optimal parameters for the reconstruction of the 3D magnetopause. BFA is effective even during rapid solar wind changes but requires a good initial guess. It also has a strong dependency on the simulation itself, since in the real-world scenario, it must fit the SXI images using only the simulation generated predictions. Further work has been done on advancing this method, leading to more sophisticated parametrization and models, such as the CMEM model [20].

The second method, proposed by Collier and Connor, is the Tangential Direction Approach (TDA) [2]. It is based on the hypothesis that the peak X-ray

intensity corresponds to the tangent line-of-sight to the magnetopause. By analyzing this intensity variation and comparing two images from nearby viewing points, the tangent point can be located. This can be thought of as a minimalistic tomographic technique, where a static magnetopause during the two images is necessary to derive meaningful information. This may be applied to cases of steady solar wind conditions, but cannot provide dynamic information, since the integration time of a single image is in the order of 10 minutes.

Finally, Sun et al. proposed a fitting scheme, based on the same hypothesis as Tangent Fitting Approach (TFA) - the tangent hypothesis [19]. In her paper, she assumes that the maximum intensity arc of the integrated image corresponds to the tangent direction of the magnetopause surface. She also verifies this hypothesis for the case of an observer at infinity (parallel integration of LOS) of an MHD emissivity cube. A secondary assumption is also necessary to transfer from a two-dimensional curve to a three-dimensional surface. Here it is proposed to assume the shape of the magnetopause by fitting empirical magnetopause models to the maximum intensity curve of the image.

The tangent hypothesis was re-examined more thoroughly by Samsonov et al. [15]. Multiple metrics for the definition of the magnetopause from the X-ray emission were tested and compared to the projection of magnetosphere's boundary in the 3D simulation cube. To extract this boundary from the simulation, they determine the magnetospheric region using the thresholds conditions for the thermal pressure and velocity. The response of the instrument is also taken into account, and a good agreement is found between the maximum gradient of intensity arc and the tangent direction of the magnetopause.

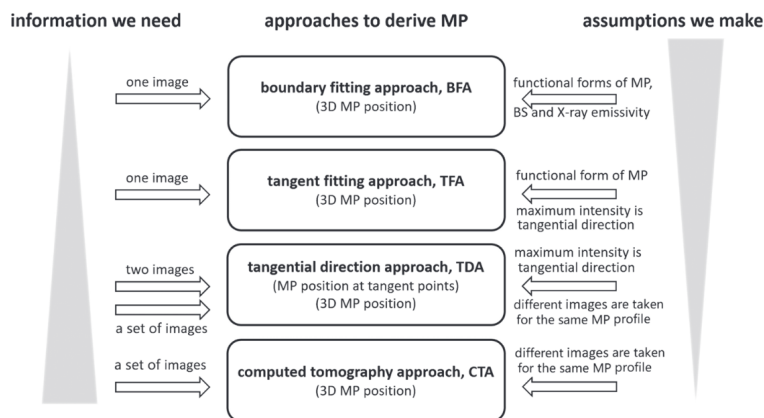


Figure 6: Magnetopause extraction techniques and their assumptions/required input [19].

It is evident that this method displays some key restrictions. Since the TFA calculates the tangent directions of the magnetopause, it is not applicable while the satellite is inside the magnetosphere. This Point Of View (POV) dependency was further studied by Read, through analyzing the validity

of the tangent hypothesis in response to different viewing geometries and satellite orbits. He shows that accurate tangent fitting strongly depends on the spacecraft's position along the orbit: only when SMILE is significantly outside the magnetopause does the peak intensity reliably trace the magnetopause tangent, while near-perigee observations fail. He also performed an interesting case study, where he generated a spherical pseudo-surface (i.e. a magnetopause proxy) to illustrate the limits of the tangent hypothesis, using a simple geometry. By applying an emissivity gradient to the pseudo-surface he demonstrated a systematic 0.3 RE error in the tangent hypothesis caused by these gradients - highlighting that spatial emissivity variations bias tangent-based fitting. This demonstrated both the orbit-dependence of the fitting accuracy and the emissivity gradients contribution to the error. This study was performed using MHD simulated emissivity cubes, while the metrics were derived using one-point (maximum intensity) comparison to the projected surface [13]. No fitting methods were developed or tested in these cases, leaving us with an estimation of the hypothesis error, but no concrete results on how this propagates to the final measurements.

We will attempt to understand the applicability of the tangent fitting method using the [LaTeP](#) model. To do that we need to examine its assumptions, consisting of two dependencies; first that the maximum integrated intensity coincides with the tangent direction of the magnetopause surface, and second that the empirical model we have chosen is a good description of its shape. We can then develop a methodology that will allow us to extract the empirical model parameters, from each [SXI](#) image, and reconstruct the 3D magnetopause. We will address these issues in the following chapters.

## THE TANGENT HYPOTHESIS

---

Although, the question of the validity of the tangent hypothesis has been tackled by previous studies, further characterization is still necessary in order to derive the limits of the tangent fitting approach. In this chapter we will study how this translates to the X-ray emissivity that has been simulated by the [LaTeP](#) model, taking into account the evolution of the orbit and attitude of the satellite. Unlike the single point approach of A. Read [13], we will attempt extracting the full maximum intensity arc of the integrated images and compare this with the projection of the magnetopause tangent that has been extracted from the simulation cubes.

### 2.1 EXTRACTING THE MAGNETOPAUSE SURFACE FROM THE SIMULATION

The extraction of the magnetopause location from the simulation requires that we understand the information that the output cubes can provide, as well as the various ways the magnetopause can be defined and derived from this information. This can be done either utilizing the electromagnetic fields of the [MHD](#) input that was given to the [LaTeP](#) model, either the X-ray production itself in the [MHD](#) or the [LaTeP](#) case.

#### 2.1.1 *LaTeP* model: Emissivity cube

The output of the simulation is in the format of Network Common Data Form ([NetCDF](#)) files containing information about the X-ray photon production of each grid point in  $[1/(cm^3 s)]$ . This is initially expressed in the local simulation coordinate system and has to be transported and interpolated into a [GSE](#) grid. In order to get the volume emissivity in  $[eV cm^{-3} s^{-1}]$  we need to take into account that the number of test particles in simulation is far less than the number of physical particles. Each test particle is assigned a weight which is proportional to the number of physical particles, so that their contribution can be converted to the one of physical particles. After deriving this weight  $w_0$ , we can determine the number of physical particles of the species  $X^{q+}$  by accounting for their relative abundance with respect to solar wind protons:

$$N_{X^{q+}} = N_{SW} \cdot \left[ \frac{X^{q+}}{O} \right] \cdot \left[ \frac{O}{H^+} \right]$$

where  $N_{SW}$  and  $N_{X^{q+}}$  represent the number of physical particles corresponding to solar wind protons and  $X^{q+}$  ions, respectively [21]. The volume emis-

sivity can therefore be derived from the production of the data cube through [Equation 15](#).

$$Q_{\text{GSE}} = P_{\text{GSE}} * w_0 * \text{abundance} \quad (15)$$

For the correct dimensionality of the integration of the emissivity along the LOS, we need to also convert the grid step to physical values, where each step corresponds to 0.05 RE

$$ds = 0.05 * R_E * 10^5 [\text{cm}]$$

We can visualize the integration from an infinitely distant POV of the Z and Y-axis through a discretized integration over them:

$$z_{\text{POV}} = \sum_z \frac{Q_{\text{GSE}}(x, y, z)}{4\pi} * ds$$

$$y_{\text{POV}} = \sum_y \frac{Q_{\text{GSE}}(x, y, z)}{4\pi} * ds$$

where we divide by  $4\pi$  to get the emissivity per steradian. The result is shown in [Figure 7](#). This results in a large dynamic range of intensities  $\in [10^{-12}, 10^6]$  eV/cm<sup>2</sup>/s/sr, with a significant contribution from the polar cusps.

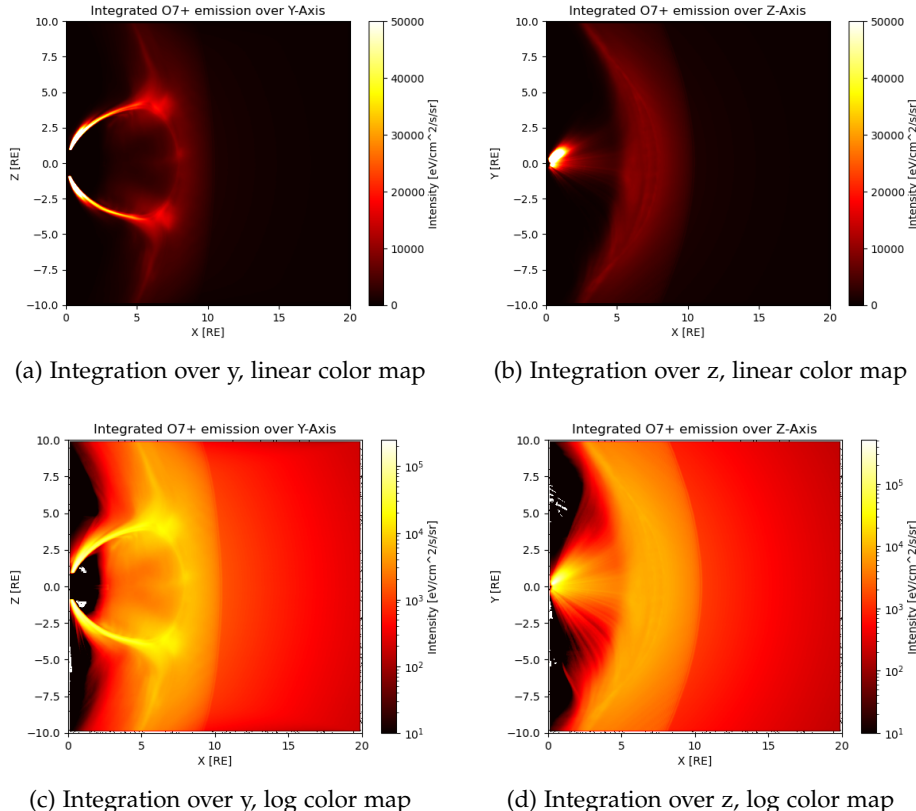


[Figure 7](#): Integration of emissivity for observers at infinity along the Z and Y-axis. The linear color map has been limited up to  $5 \cdot 10^4$  eV/cm<sup>2</sup>/s/sr, while the logarithmic has a lower limit of  $10$  eV/cm<sup>2</sup>/s/sr.

It is apparent that the study of the tangent hypothesis even for the simple case of an observer at infinity as studied by Sun et al., is not as straight forward for the test particle model. The smooth gradients of purely MHD models greatly simplify the process of extracting the maximum intensity arc, whereas the kinetic effects of the LaTeP model introduce prominent structures, jumps and contribution form the cusps.

We can run a test to verify this by comparing the maximum intensity per line to the projection of the MHD input mangetopause. We extract the latter for the  $z = 0$  slice of the MHD input cube, by finding the boundary of the closed magnetic field lines. Additionally, we can mask a 4RE radius sphere to reject the low altitude cusp contribution. The result is shown in Figure 8, where the blue dashed line is the maximum intensity and the red line the projected closed field line boundary. The black line represents the Shue model, constructed from the input parameters of the OpenGGCM simulation (Table 1).

PARAMETER	VALUE
IMF $B_z$	-5 nT
SW Velocity $v_x$	-400 m/s
SW Density $n$	12.5 1/cm <sup>3</sup>
SW Dynamic Pressure $P_{Dy,n}$	3.84 nPa

Table 1: Initial OpenGGCM simulation parameters.

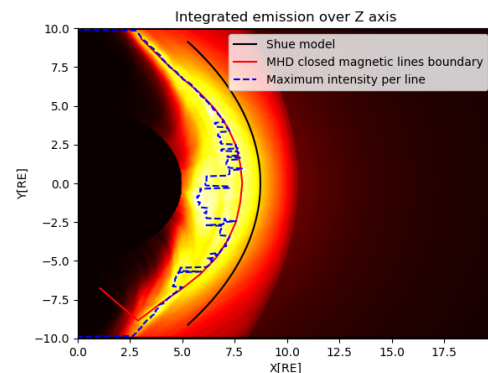


Figure 8: Integration over z.

Although at the edges, the projected magnetopause coincides with the maximum intensity, the contribution of the cusps extends further than the mask at low polar angles and the two lines significantly deviate. The parametrization of the Shue model also does not represent this simulation, meaning that there is no agreement between the simulation parameters and the subsolar distance  $r_0$  the shue model estimates. This however does not mean we cannot still utilize the model as a purely geometrical description.

### 2.1.2 Shue model fitted to slices

We can extract some information about the shape and position of the simulation's magnetopause by analyzing the emissivity cubes themselves. It is expected that the absence of the solar wind inside the magnetosphere will result to zero - or almost zero- emissivity of X-rays in this region. Since the magnetopause is by definition the barrier that separates the magnetosphere from the solar wind, we can take the (almost) zero contour of a slice as the definition of the magnetosphere limit, meaning the magnetopause. We should keep in mind, however, that in reality the magnetopause is not an

infinitely thin surface and further metrics could be used to define it. We will utilize such metrics in our next attempts to extract the surface as well.

We analyze two key slices of the emissivity cubes, the  $z = 0$  and  $y = 0$  slice, and extract the zero contour from their 2D contour maps. We convert these contour curves to polar coordinates, as drawn with the red line in [Figure 9](#). We are now in a spherical system as defined in [Section 1.3.1.1](#) where  $z$  slice corresponds to  $\phi = 0^\circ$  and the  $y$  slice to  $\phi = 90^\circ$ .

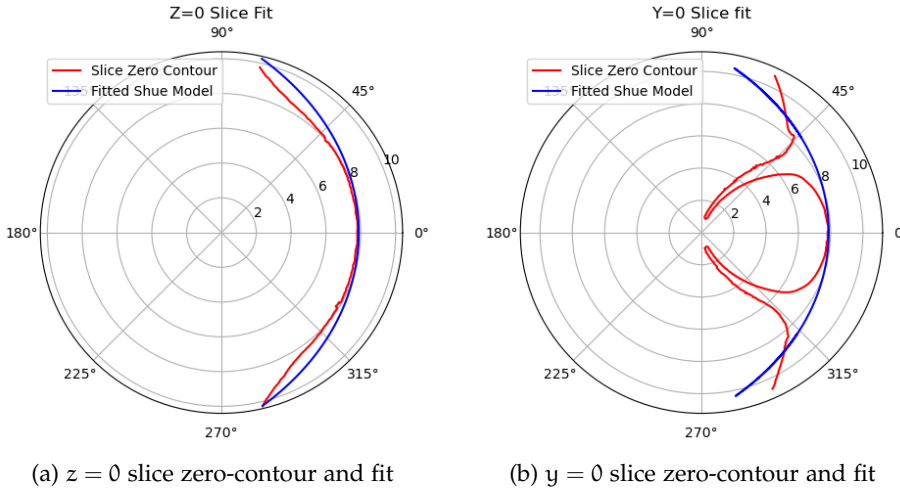


Figure 9: Zero-contour lines and the corresponding fitted Shue model

The Shue model is the most simplistic description of the magnetopause, accounting for no asymmetries or indentations, and having full rotational symmetry over the GSE x-axis. Therefore, its full spherical expression will remain unchanged:

$$r(\theta, \phi) = r_0 \left( \frac{2}{1 + \cos \theta} \right)^\alpha \quad (16)$$

where  $r_0$  is the subsolar distance and  $\alpha$  a shape parameter that determines the flaring.

We can approximate the  $\phi = 0$  slice of the magnetopause by best fitting these parameters to the zero emissivity contour slice. The asymmetries and indentation introduced by the cusps in the  $y$  slice, cannot be described by this model, as seen in [Figure 9b](#). Nonetheless, we will use this fitted model as first approximation of the 3D surface of the simulated magnetopause. The parameters have been estimated to:

$$r_0 = 7.82 \text{ RE}$$

$$\alpha = 0.386$$

### 2.1.3 Radial extraction of full magnetopause

Extracting the zero contours through the contour maps of each slice would be a tedious task. To obtain the full surface information we can instead trans-

fer the emissivity cube from the GSE to spherical coordinates in order to treat each radial direction separately. A script for this transformation was provided by Samuel Wharton (SXI team, University of Leicester) and is part of his work on the CMEM model[20]. The result is the same emissivity cube, but instead of 3D array representing each dimension of the box ( $x$ ,  $y$ ,  $z$ ) we have discretized  $\phi \in [0, 360]^\circ$  and  $\theta \in [-65, 65]^\circ$  with a step of  $0.5^\circ$  and  $r \in [0, 15]$  RE with a step of 0.2 RE. We did not let  $\theta$  range all the way to  $\pi/2$  since there is no physical information from the simulation box in that region. The result can be seen in [Figure 10](#), where the spherical slices corresponding to the GSE  $y = 0$  and  $z = 0$  cuts are plotted.

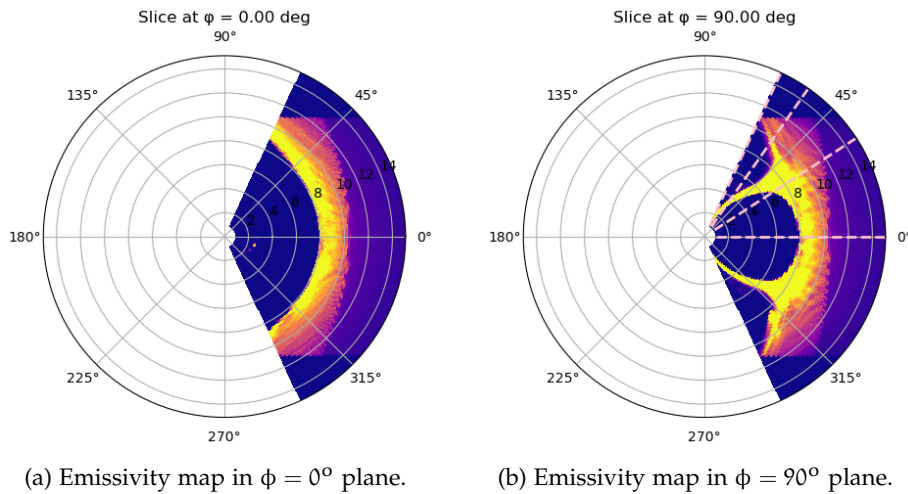


[Figure 10](#): Emissivity cube slices in spherical coordinates. The  $\theta$  directions of [Figure 11](#) are denoted with the dotted lines.

To better understand the radial profile of the volume emissivity, we plot it versus the radius for different polar  $\theta$  directions in [Figure 11](#).

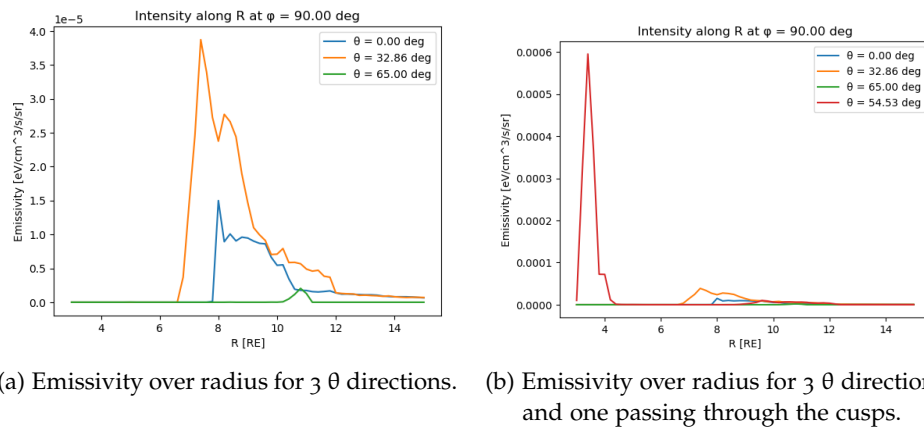


[Figure 11](#): Emissivity over radius for different  $\theta$  directions in the  $\phi = 90^\circ$  plane

The  $\phi = 90^\circ$  plane was chosen since it is the one displaying more complex behavior due to the cusps. The typical behavior near the subsolar point

is shown in [Figure 11a](#), where a steep increase appears at the edge of the magnetosphere, forming a global maximum in the X-ray emissivity. In [Figure 11b](#) the same directions are plotted, along with  $\theta = 54^\circ$  which crosses the polar cusp. We can see that the emissivity of this region is significantly prominent, overshadowing the second peak that appears close to the outer boundary of the magnetosphere.

In previous work, various diagnostics of this curve have been used to define the magnetopause surface, such as the global maximum[[19](#)], the maximum gradient[[15](#)], as well as the quarter of the distance between the maximum gradient and the global maximum [[13](#)]. The shape of the magnetopause is not significantly affected by this choice. Since our goal in this section is to eventually test the tangent hypothesis, the maximum emissivity is a more suitable metric to compare to the integrated maximum intensity curve.

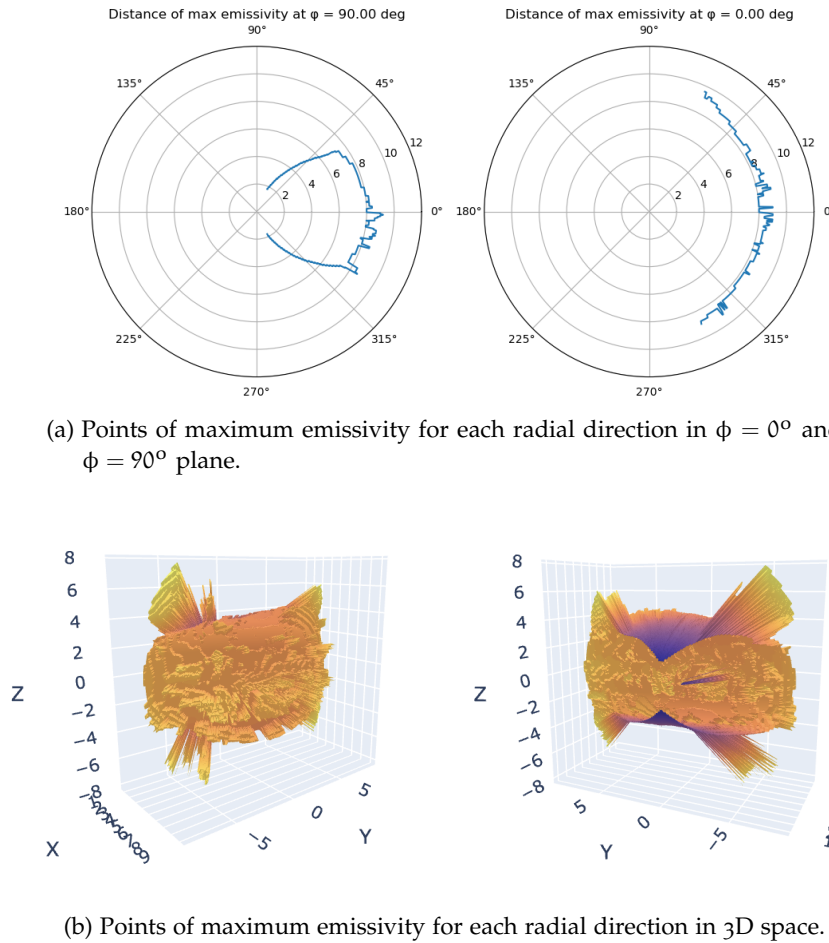


[Figure 12](#): Extraction of maximum emissivity surface from the LaTeP cube.

We can find the indexes of the maximum emissivity of each radial direction and plot them both as slices and as a 3D surface, as in [Figure 12](#). It is evident that a lot of information is being obscured by the cusp's maxima and their inward curvature. The peaks characterizing the outer boundary of

the magnetosphere are not registered, as the cusps act as a "wall" for those radial directions.

To bypass this problem, we tried to utilize the difference of magnitude of the emissivity in the cusps and the outer boundary, by finding all the peaks of the radial emissivity and keeping only those that are below an arbitrary threshold of  $1e - 5\text{eV/cm}^3/\text{s/sr}$ . This improves the results to some extent, but is not a robust enough definition to result in a continuous and coherent surface.

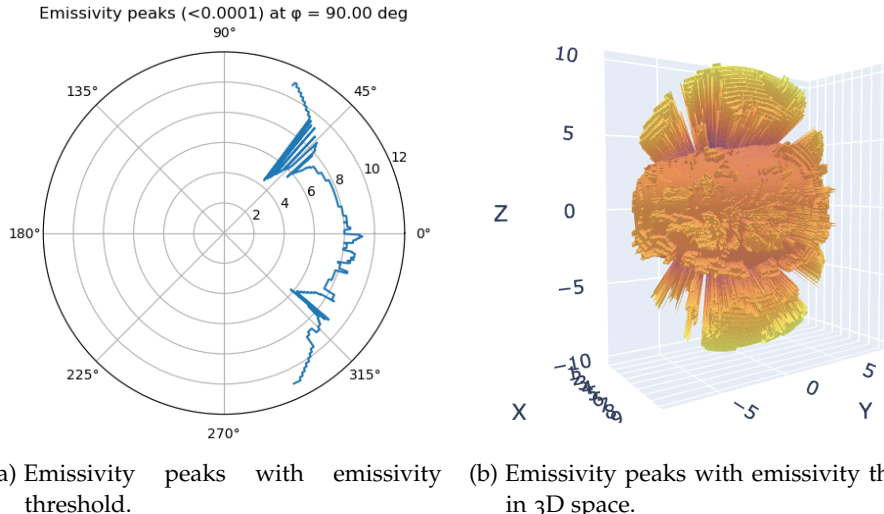


Figure 13: Extraction of emissivity peaks below an emissivity threshold surface from the LaTeP cube.

Finally, we tried setting a lower limit to the radius of the maximum, to avoid some jumps to very low altitudes, which were mostly the result of simulation discontinuities.

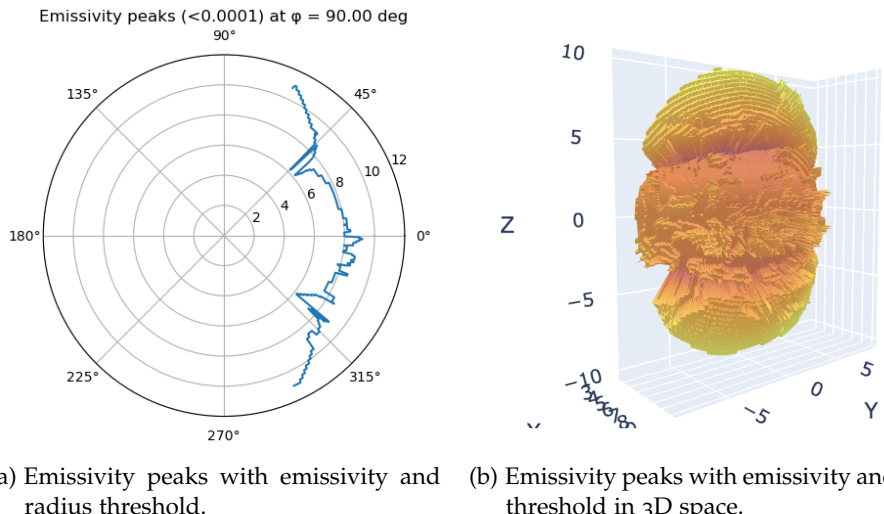


Figure 14: Extraction of emissivity peaks below an emissivity and above a radius threshold surface from the LaTeP cube.

The result is again better, however quite a few arbitrary thresholds have been introduced to achieve it. At the same time, the smaller jumps due to the nature of the particle simulation have not been addressed. To deal with these discontinuities, we attempted to smooth the surface, however their regular appearance results to a highly variable smoothed surface.

Extracting a smooth surface using diagnostics from the particle simulation proved to be a challenging task. This is not something that can be mitigated by choosing a better diagnostic, since the nature of the simulation itself results in unavoidable discontinuities and stochastic jumps. This leaves us with two possible solutions: Either to utilize the input MHD information that was provided to the LaTeP model, either to fit empirical models to the surface we have extracted from the particle model directly.

#### 2.1.4 Fitting models to surface

In his series of papers studying and comparing various magnetopause empirical models, Nguyen et al. defines numerically these models in a publicly available [script](#). We will use some of these functions to understand whether they could describe the simulation's magnetopause. We will be initializing each of the following fits with the simulation parameters as indicated in [Table 1](#). For the parameter estimation we will use directly the built-in curve-fit function of SciPy.

In [Figure 15a](#) we have tried fitting the Shue model to the full 3D data of the maximum emissivity surface. The estimated parameters were the following:

PHYSICAL PARAMETERS	GEOMETRIC PARAMETERS
$P_{dyn} = 11.354 \pm 0.008 \text{ nPa}$	$r_0 = 8.67 \text{ RE}$
$B_z = 6.822 \pm 0.11 \text{ nT}$	$\alpha = 0.6$
RMSE = 1 RE	

Table 2: Shue model parameters, fitted to LaTeP maximum emissivity surface.

As expected, the Shue model cannot accurately describe the surface, rather it fits to the cusps instead of capturing the outer boundary.

The same process was implemented for the Lin model, which accounts for a significant indentation due to the cusps. However, as seen in [Figure 15b](#) the indentation is a localized feature that does not seem to describe the geometry of the extracted surface. The pressures do not converge, and we end up with a significant error both in their estimation and the final Root Mean Square (RMSE).

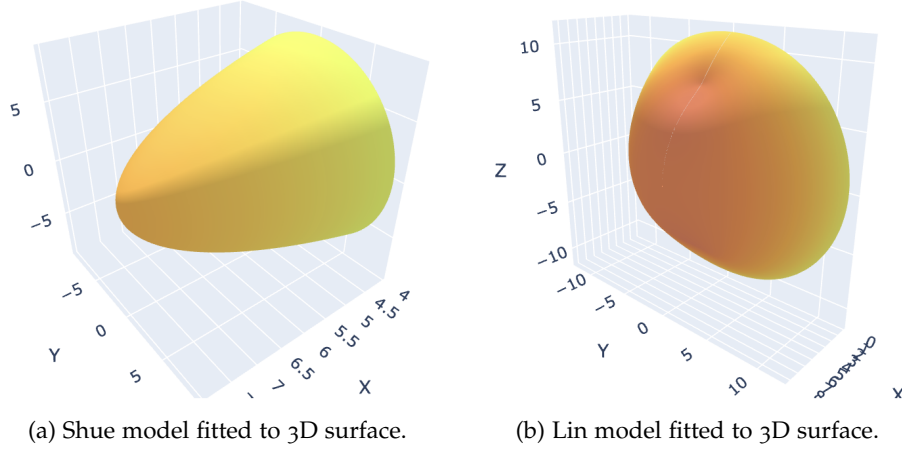


Figure 15: Shue and Lin model fitted to the maximum emissivity surface extracted from LaTeP.

PHYSICAL PARAMETERS	GEOMETRIC PARAMETERS
$P_{dyn} = 4.12 \pm 11674 \text{ nPa}$	$r_0 = 8.49 \text{ RE}$
$P_m = 0 \pm 11674 \text{ nPa}$	$\alpha(\phi)$
$B_z = -7.7 \pm 0.05 \text{ nT}$	$Q(\theta, \phi)$
RMSE = 0.58 RE	

Table 3: Lin model parameters, fitted to LaTeP maximum emissivity surface.

Finally, we attempted to fit the Liu model, which is a more resembling geometry of the original surface. The model could not predict the positions of the cusps to be so close to the subsolar point, and ended up fitting the entire [-65,65] degrees domain of our data as the front lobe of the magnetopause.

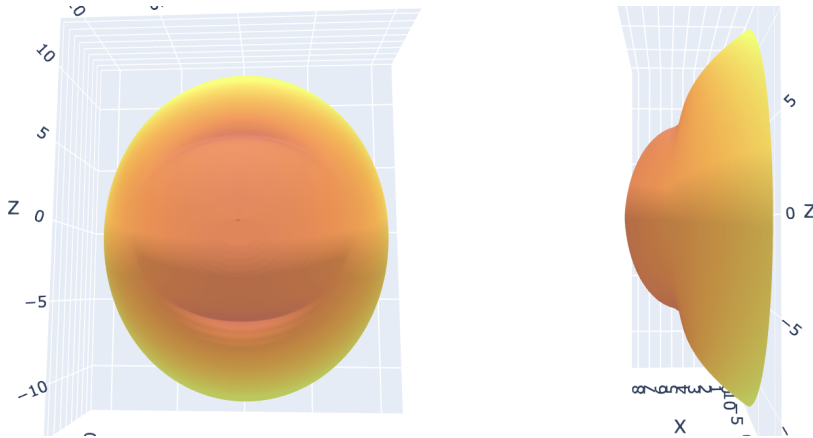


Figure 16: Liu model fitted to the maximum emissivity surface extracted from LaTeP.

PHYSICAL PARAMETERS	GEOMETRIC PARAMETERS
$P_{dyn} = 6.05 \pm 0.8 \text{ nPa}$	$r_0 = 8.3 \text{ RE}$
$P_m = 0 \pm 0.8 \text{ nPa}$	$\alpha(\phi)$
$B_z = -5.45 \pm 0.01 \text{ nT}$	$Q(\theta, \phi)$
RMSE = 0.7 RE	

Table 4: Liu model parameters, fitted to LaTeP maximum emissivity surface.

Even if we ignore the shape differences of the models with our simulation data as an approximation, the large contribution from the jumps of the maximum emissivity does not allow for reliable fits. All the above models, when fitted, overestimated the subsolar distance, since the contribution of the jumps is non-negligible. Simultaneously, errors of the order of 1 RE cannot be neglected when we are trying to verify the tangent hypothesis, in order to utilize it for sub-RE detection of the magnetopause.

#### 2.1.5 Extracting the magnetopause from the MHD emissivity

Instead of trying to smooth the LaTeP surface and deal with the discrete nature of the particle simulation, it would suffice to show that the maximum emissivity calculated from the MHD input coincides with the mean maximum curve of the particle model. This is to be expected, since the particles follow the motion dictated by the input fields and the position of the magnetopause should be able to be defined both by the field and the emissivity interchangeably. The XY and XZ slices of the MHD emissivity cube are shown in [Figure 17](#) in spherical coordinates.

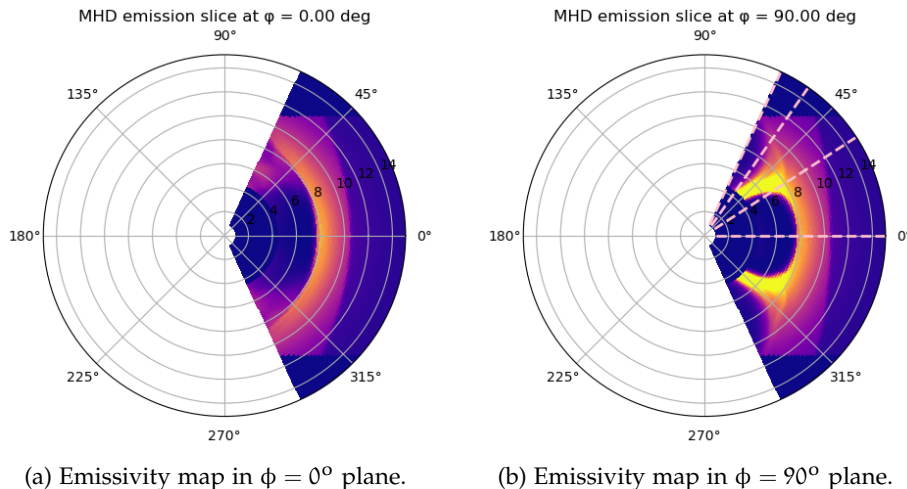
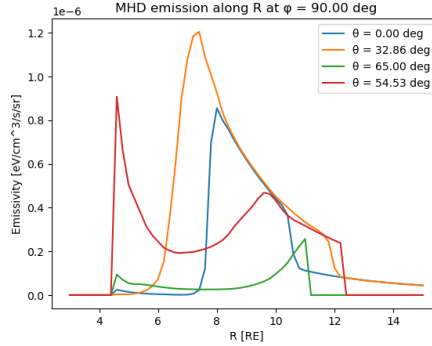


Figure 17: MHD emissivity cube slices in spherical coordinates. The  $\theta$  directions of [Figure 18](#) are denoted with the dotted lines.

To better understand the radial profile of the emissivity, we plot it versus the radius for different polar  $\theta$  directions in [Figure 18](#). We notice similar peaks as in the LaTeP case ([Figure 11](#)) but with much smoother behavior as well as moderate contribution from the cusps, particularly due to the mask that is applied to remove the artificial inner-magnetosphere emission at  $R \leq 4$  RE.



(a) Emissivity over radius for 4  $\theta$  directions.

[Figure 18](#): MHD emissivity over radius for different  $\theta$  directions in the  $\phi = 90^\circ$  plane

By following the previous methods, we can extract the maximum intensity per radial direction and plot it as a surface in [Figure 19](#). Comparing to [Figure 12](#) this returns a smoother surface and further points away from the cusps. We can also try to limit the radial extend of the cusps to above 5 RE, and thus gain more information on the directions that are blocked by them ([Figure 19b](#)).

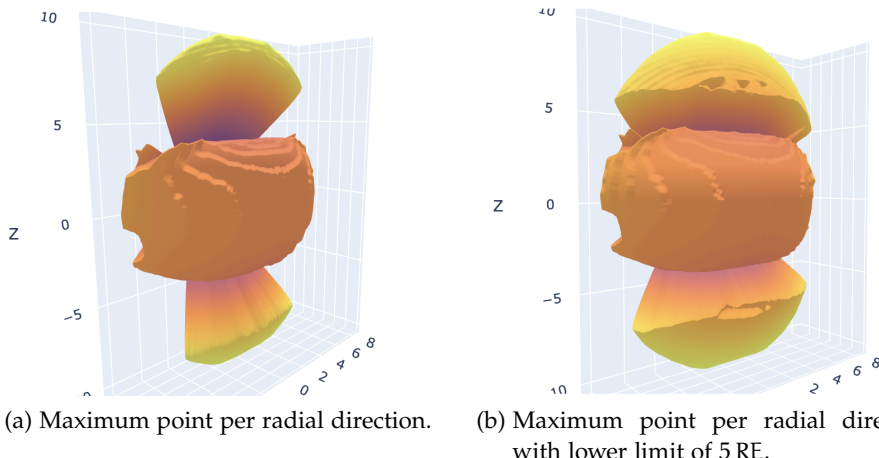
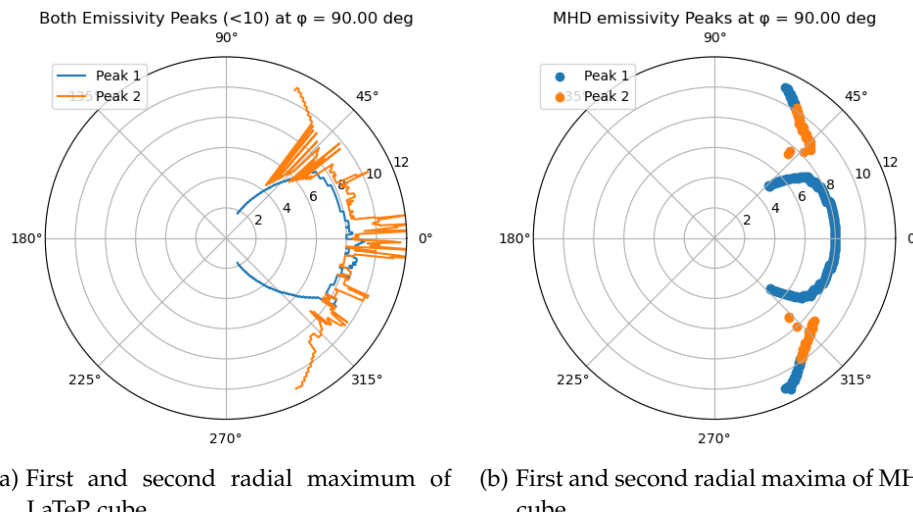


[Figure 19](#): 3D surfaces extracted from MHD emissivity cube.

We can understand further the structured and discontinuous features of the LaTeP surface by examining [Figure 20](#). Here we plot both the global maximum peak, and the second maximum. In the MHD case, the second peak is indeed detected in the outer boundary of the magnetopause, and can be uti-

lized to construct a surface without the problem of obscuring some points by the curvature of the cusps. In the LaTeP case, the second peak jumps from one boundary to another and oftentimes overshoots for the directions that we do not have two physical maxima. This is caused by the "bumpy" behavior of the radial profiles, meaning that small disturbances along the first maximum will be counted as a higher peak than the second maximum. This also causes the overshoot of the subsolar distance when fitting empirical models to the LaTeP surface. By limiting the radial maxima as well as the magnitude, we have essentially forced it to jump to these bumps for certain directions, resulting in an even higher variability in the surface, than if we took the total maximum. This could potentially be mitigated by smoothing the radial profiles before extracting the maxima.



(a) First and second radial maximum of LaTeP cube.  
(b) First and second radial maxima of MHD cube.

Figure 20: MHD emissivity over radius for different  $\theta$  directions in the  $\phi = 90^\circ$  plane

Moving back to the analysis of the MHD cube, we can utilize the smooth behavior seen in Figure 20b to construct a surface where we keep both the first and second maxima, keeping both the information about the strong indentation and the outer boundary. This is plotted in Figure 21.

## 2.2 EXTRACTING THE MAXIMUM INTENSITY CURVE FROM THE IMAGE

As suspected from Figure 8 the extraction of the maximum intensity arc is not as trivial as in the smooth-gradient MHD case. This will not change when introducing the [SXI FOV](#) and the satellite's [POV](#), but it will improve since the instrument never points directly to the cusps, while image processing techniques can also be applied to extract continuous arcs.

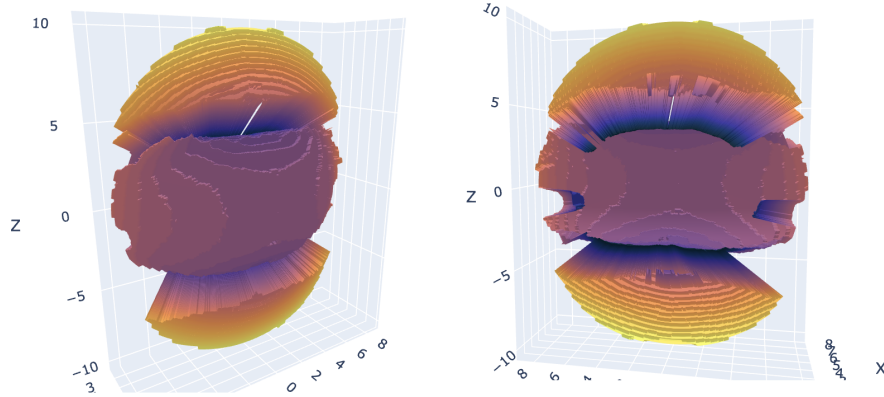


Figure 21: Final magnetopause surface. First and Second maxima peaks of MHD emissivity cubes.

### 2.2.1 Constructing the images

To construct the synthetic images of the [SXI](#) instrument, we use the [3DView](#) open-source tool developed by CDPP [4]. Through this tool we can simulate the orbit and attitude of the satellite for a specified interval, as well as the orientation and characteristics of the imaging system in relation to the satellite. We can directly import the emissivity cubes of the simulations, introduce the satellite and the [FOV](#) of the imager, and compute the integrated flux over each pixel's [LOS](#). We therefore get the integrated images from each [POV](#) of the orbit, according to the [FOV](#) and resolution of the imager, as shown in [Figure 22](#). No simulated noise has been added to account for the detection system of the instrument or the background contribution. A typical synthetic image of the magnetopause, generated through this method, is shown in [Figure 23a](#).

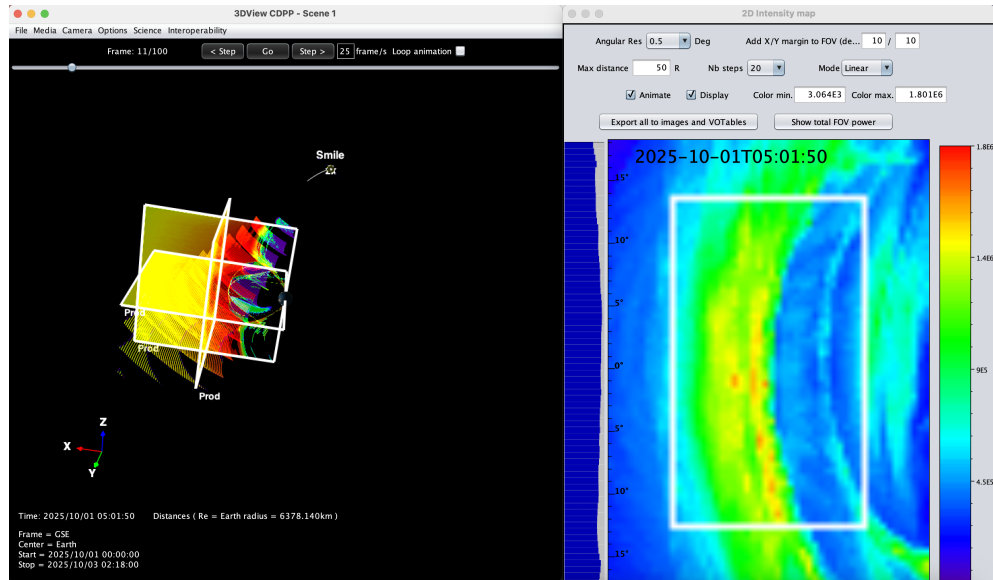


Figure 22: 3D View CDPP software

Along with the images, we can export XML files that contain information about the position and orientation of the satellite, for each time-step. This will be particularly useful in [Section 2.3](#).

### 2.2.2 Image processing

Looking at the images, we notice that two arcs seem to form, the outer one being less distinct. We will refer to that as the second maxima arc, as this second peak is observed consistently when tracing the intensity evolution over the azimuth angles for each row as seen in [Figure 23b](#). This shall not be confused with the second emissivity maximum described in the previous section, where we were referring to the 3D structures of the emissivity.

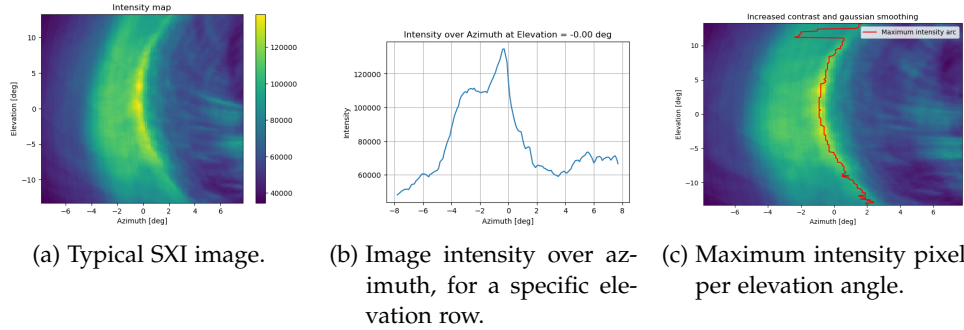


Figure 23: Typical behavior of SXI images.

If we attempt to trace the maximum pixel per row-elevation angle, we will notice prominent jumps from the maximum intensity arc to the second maximum, especially towards the edges where the intensity of the inner arc drops relative to the outer one, as in [Figure 23c](#). Attempts to discard the jumps directly proved unsuccessful since the limit in the azimuth step between rows simply slowly moved the curve to the outer arc.

Another approach to discard the jumps and limit ourselves to the arcs of interest would be to fit a polynomial to the noisy line. When trying to fit a 2nd polynomial, we have 3 degrees of freedom and therefore a 3 dimensional parameter space.

$$x = A(y - B)^2 + C$$

This is relatively fast but cannot take into account the asymmetry of the true arc ([Figure 24a](#)). If we introduce a  $y^3$  term, this anisotropy can theoretically be fitted, although in practice the 3rd order term blows up, and the resulting curve rarely converges (even with very small initial coefficients given, as in [Figure 24b](#) and [Figure 24c](#)).

Shortly, it is evident that not only is it a slow solution and without a measure of the error - but it is also difficult to implement while ensuring convergence and not overfitting. Thus, we move back to the maximum extraction for each line approach, where we need to discard the noise that causes the jumps.

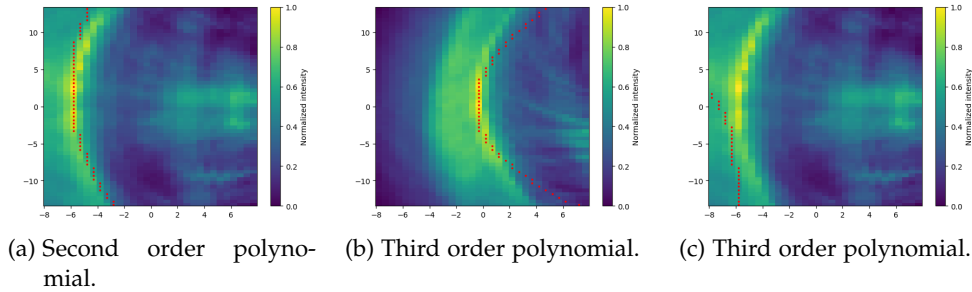


Figure 24: Polynomials fitted to noisy maximum intensity arc.

There are several image processing tools and libraries that can aide us in smoothing the image or increasing the contrast to reduce the noise and make some features more distinct. Here we increase the contrast of the images using the `skimage` library and apply a 1 sigma Gaussian filter to smooth the noise. We then find the maximum azimuth index for each elevation and discard the ones that have a jump larger than 2 indexes. In the pictures approaching the magnetopause random arcs are being detected, so we discard the filtered array that are smaller than 20 points (the rest have been discarded due to jumps), as well as the ones that have an average intensity smaller than 0.2 normalized, since low intensities are expected inside the magnetopause. The result is shown in [Figure 25a](#).

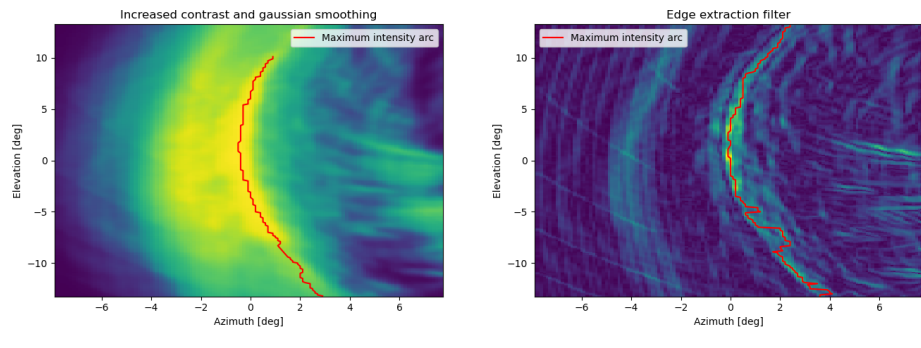


Figure 25: Arc detection after different filters and imaging processing techniques have been applied.

We can apply a similar procedure to derive diagnostics about the maximum gradient arc as well. We do this by passing the images through an edge detection filter - `skimage.filters.sobel` - which by definition extracts the maximum gradients in an image. A typical image after this filter is shown in [Figure 25b](#).

### 2.3 CHARACTERIZING THE TANGENT HYPOTHESIS

We now have a diagnostic of the maximum intensity arc of the image as well as the maximum gradient. We can compare these arcs with the projection of the tangent direction of the magnetopause surface we have extracted from the simulation, to understand if we can derive a correlation.

#### 2.3.1 Projecting the surface

Since we have extracted the numerical surface in spherical coordinates, we can also find the points that correspond to the tangent direction and project them into the FOV of the instrument. Let's suppose that for a particular image, the satellite is located at the position  $\vec{r}_{\text{sat}} = (x_{\text{sat}}, y_{\text{sat}}, z_{\text{sat}})$  in the GSE system. The tangent points of the surface for this location will satisfy the condition:

$$\vec{n} \cdot (\vec{r}_{\text{point}} - \vec{r}_{\text{sat}}) = 0 \quad (17)$$

where  $\vec{r}_{\text{point}}$  is the position of each point of the numerical surface and  $\vec{n}$  is the normal vector of the surface for each point, in the GSE system. We can get  $\vec{r}_{\text{point}}$  by simply applying the transformation from the spherical system to the cartesian as defined in [Section 1.3.1.1](#). To get the normal vectors, we calculate the gradient of the surface with respect to  $\theta$  and  $\phi$  and normalize the corresponding vectors. We can calculate the normals for each point through their cross product:

$$\vec{n} = \frac{\partial \vec{r}}{\partial \theta} \times \frac{\partial \vec{r}}{\partial \phi} \quad (18)$$

To get the tangent curve, we simply solve [Equation 17](#) numerically, to get the points that satisfy it. In our case, we applied a simple mask with an arbitrary threshold of  $0.05^\circ$  tolerance, as a first approximate and fast solution.

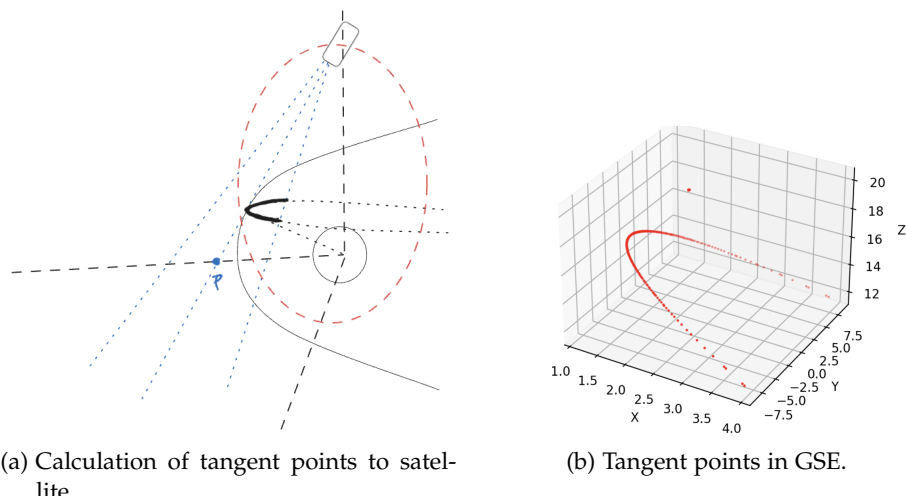


Figure 26: Extraction of tangent point to satellite for a numerical surface.

The orientation of the satellite is described by three vectors, giving each base vector of the satellite coordinate system, expressed in the [GSE](#) frame. To move from one system to another, it is sufficient to define the rotation matrix through these vectors and apply a translation according to the position of the [satellite](#), meaning the origin of the satellite's coordinate system. We construct the rotation matrix:

$$R = \begin{bmatrix} | & | & | \\ e_x^{\text{sat}} & e_y^{\text{sat}} & e_z^{\text{sat}} \\ | & | & | \end{bmatrix}$$

The relation between a vector in the [GSE](#) frame and the same vector in the satellite frame is:

$$\vec{r}_{\text{GSE}} = R \cdot \vec{r}_{\text{SF}} + \vec{t} \quad (19)$$

where  $r_{\text{SF}}$  is the vector of a point in the satellite frame and  $\vec{t}$  is the translation vector. Therefore, the transformation of a point in [GSE](#) to the satellite frame is performed by the following operation:

$$\vec{v}_{\text{sat}} = R^\top \cdot (\vec{v}_{\text{GSE}} - \vec{t})$$

In order to project this in the [SXI](#) coordinates we need to compute the angle of each point from the z axis (boresight) along the x and y direction of the satellite frame:

$$\text{azimuth} = \arctan \frac{x}{z}$$

$$\text{elevation} = \arctan \frac{y}{z}$$

And limit this to the [FOV](#) of the imager, with  $\text{azimuth} \in [-7.8, 7.7]^\circ$  and  $\text{elevation} \in [-13.2, 13.2]^\circ$ . We can also define a coordinate transformation from the [SXI](#) degree coordinates to the indexes of the image, by mapping these angles to grid indices  $i_{\text{az}}$  and  $i_{\text{el}}$ :

$$i_{\text{az}} = \text{round} \left( \frac{\theta_{\text{az}} - \text{Azmin}}{\text{Azmax} - \text{Azmin}} \cdot (\text{Naz} - 1) \right)$$

$$i_{\text{el}} = \text{round} \left( \frac{\theta_{\text{el}} - \text{Elmin}}{\text{Elmax} - \text{Elmin}} \cdot (\text{Nel} - 1) \right)$$

where  $\text{Naz}$  and  $\text{Nel}$  are the number of azimuth and elevation grid points, respectively. To ensure the indices stay within valid bounds we also clip to the minimum of the grid:

$$i_{\text{az}} = \min(\max(i_{\text{az}}, 0), \text{Naz} - 1)$$

$$i_{\text{el}} = \min(\max(i_{\text{el}}, 0), \text{Nel} - 1)$$

### 2.3.2 Results: Characterizing the Tangent Hypothesis

We can now derive diagnostics about the correlation of the maximum intensity curve of the image and the projected tangent points of the surface. We do this by calculating the RMSE between the two curves of each image. By taking a sequence of images over some key orbits we can understand how this error evolves depending on the geometry of observation. We run this test for a full orbit ( $T = 50.3$  hours) per month, from June 2025 to May 2026. As described in [Section 1.3.2.2](#), the orbit has an inclination of  $73^\circ$ , however the orientation of this inclination precesses and thus the geometry of observation changes seasonally. This in turn affects the projection of the magnetopause to the FOV as well as the tracing of the maximum intensity arc. We will look into this seasonal dependency of the tangent hypothesis, and will point out its limitations.

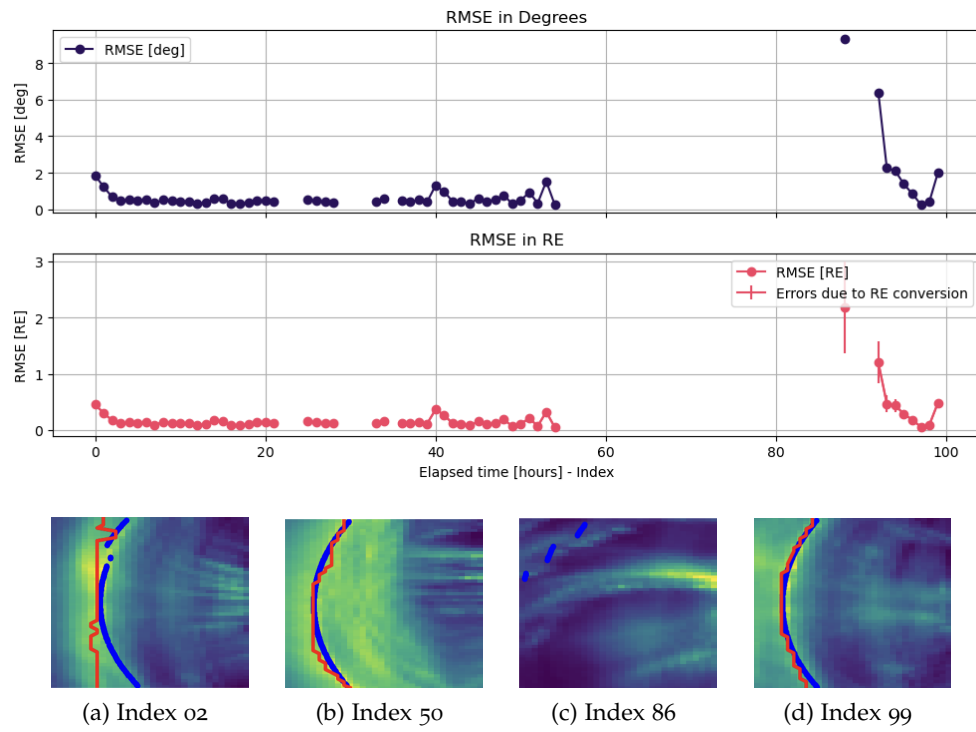
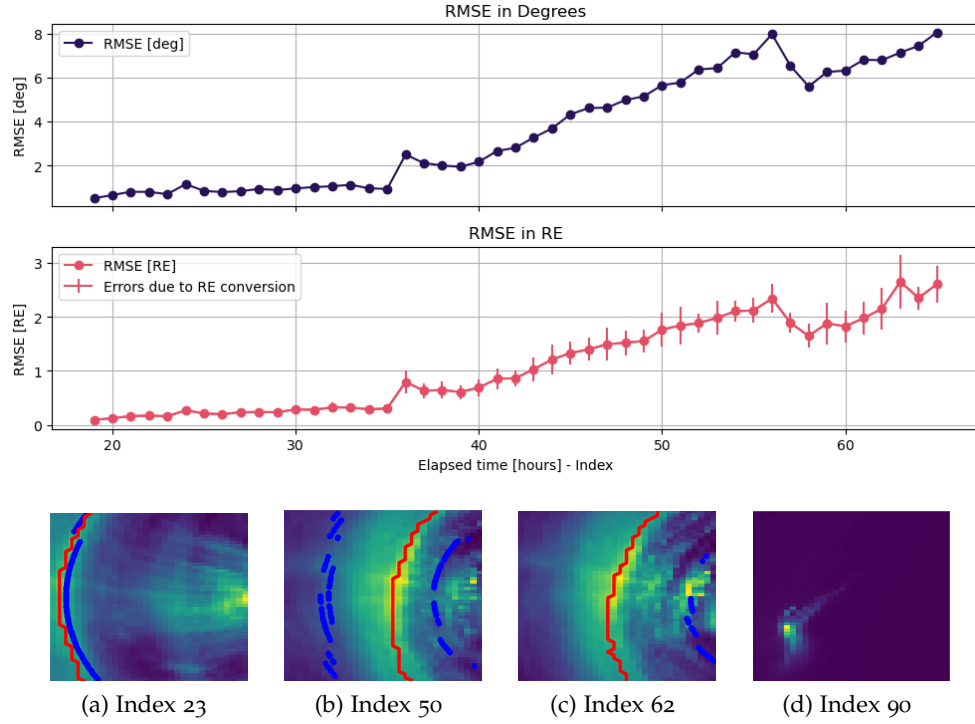


Figure 27: Evolution of RMSE over time elapsed from 2 June 2025 00:00 UTC and key snapshots. Magnetopause projection is indicated in blue while the red curve indicates the detected maximum intensity arc.

In [Figure 27](#) we see the evolution of the RMSE over a summer orbit in June 2025. The agreement between the projection of the magnetopause surface, indicated with the blue points, and the maximum intensity arc of the image, indicated with the red line, is close to 0.1 RE for most of the orbit, going sufficiently below the 0.5 RE error that was set as a requirement for the SXI instrument. An example of a good agreement is shown in the snapshot of [Figure 27b](#) and [Figure 27d](#). We also observe cases where the error peaks, as in [Figure 27a](#), where although the projection seems correct, the extraction of the

maximum intensity line fails to capture the intended curve. Finally, we show an example of the satellite entering the magnetopause in [Figure 27c](#), where no curve can be detected since the emissivity inside the magnetosphere is zero. In such cases we discard the measurement since this is a clear limitation of the [TFA](#).



[Figure 28](#): Evolution of RMSE over time elapsed from 1st November 2025 00:00 UTC and key snapshots.

Moving to the winter months, we no longer have problems with tracing the maximum intensity line, however certain [POVs](#) show a clear problem with the magnetopause surface and its projection to the [FOV](#). [Figure 28b](#) and [Figure 28c](#) show two cases where the projection shows no correlation with the expected shape. The inner arc is a projection of the indentation of the cusps. Our grid is quite sparse for such a rapid indentation, leading to not representative gradients of the surface, at the point of the discontinuity. However, this also shows our inability to correlate the projection of the cusps with a distinct geometric feature of the images. Although the cusps are highly luminous, they are also localized, meaning that their emission is not integrated over a significant portion of the [LOS](#). This results in structures that are noticeable in the integrated image, but not prominent or consistent enough to allow for the correlation of their projection with their position. In any case, the concept of the tangent hypothesis has its foundation on the integration of a relatively homogeneous emission over the maximum path - excluding thus bright but localized features.

The outer arc projection seen in [Figure 28b](#) is more difficult to interpret, and the orbit of the satellite during the winter months should be taken into

account. To understand this projection, we shall take a look at the viewing angle of the 3D magnetopause surface, as shown in the summary of the projection problem in [Figure 30](#). The interpretation of the inner arc clearly agrees with the projection of cusps here. The outer tangent to the surface however, seems to severely overestimate the position of the maximum intensity arc. This can be explained by going back to the conclusion Read reached in his paper, where he examined a spherical homogeneously emitting surface and found the tangent hypothesis to hold true. However, when he introduced gradients to the emission, making some regions more luminous than others, the maximum intensity arc consistently underestimated the position of the tangent arc [\[13\]](#). It is also known that the subsolar point will be significantly more luminous than higher latitudes, due to the flux of the solar wind. The contribution from the integration of the high latitude emission is not enough to counter the emission gradient near the subsolar point, leading to the underestimation of the tangent position when the satellite exceeds a certain latitude. This is reflected in the correlation of this phenomenon with the winter orbits ([Figure 31b](#)), as well as with the polar angle of the position of the satellite. We show this correlation in [Figure 32a](#), and we will further discuss it below.

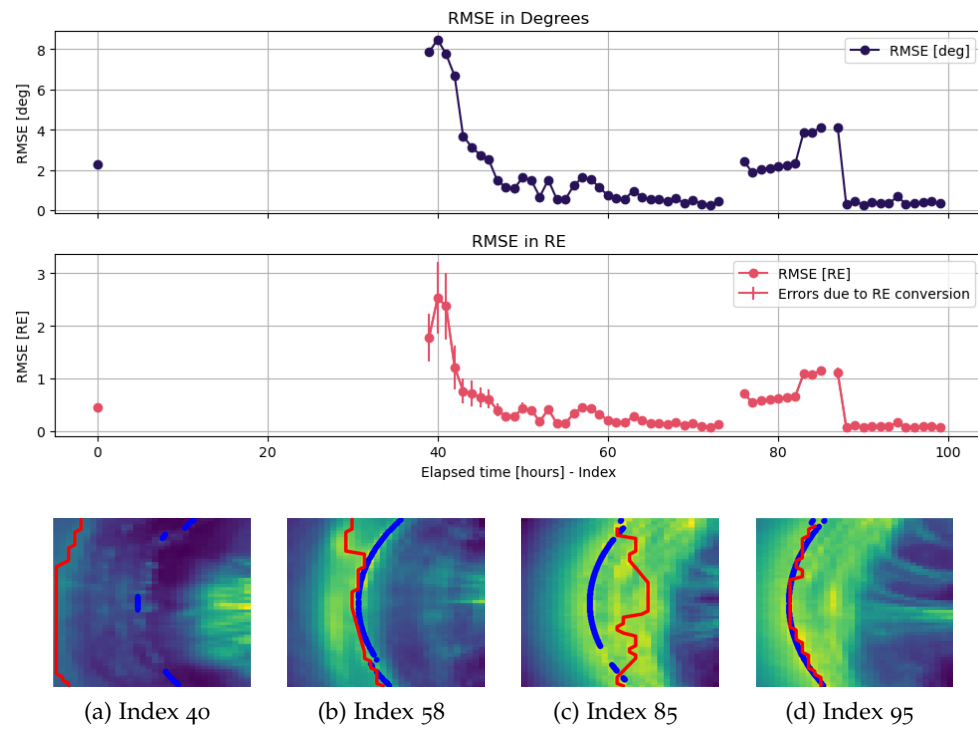


[Figure 29](#): Evolution of RMSE over time elapsed from 1st April 2026 00:00 UTC and key snapshots.

Looking into another summer orbit, during April 2026 ([Figure 29](#)), we observe similar behavior with June 2025, where the projection of the surface displays no surprising components, however the extraction of the maximum intensity arc oftentimes fails. This is strongly correlated with the inclina-

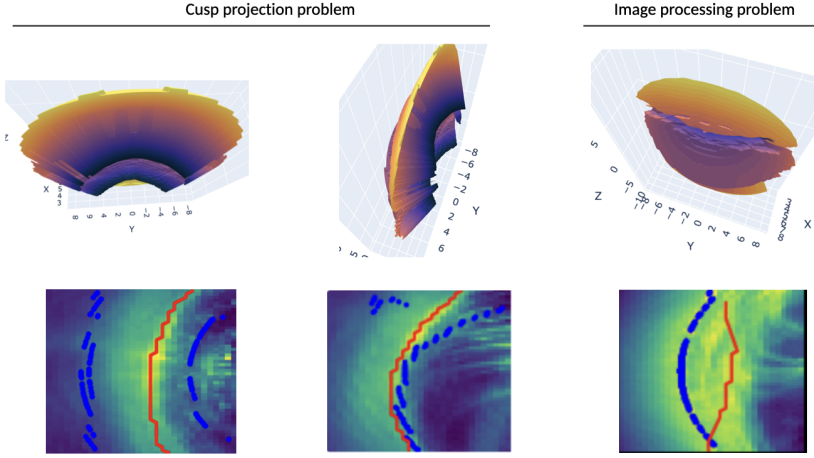


Figure 30: Viewing direction correlated with surface projection and image processing problems

tion during these months and the resulting [POVs](#). [Figure 30](#) shows the corresponding viewing angles of the 3D surface for arc extraction problem. The contribution to the intensity of every part of the surface, makes it difficult to track a single and distinct maximum intensity arc. This is clearly reflected in the integrated image of [Figure 29c](#), where the previously distinct arc is no longer a thin line. A representative orbit during the summer months is shown in [Figure 31c](#), where X is the axis towards the sun in the GSE system.

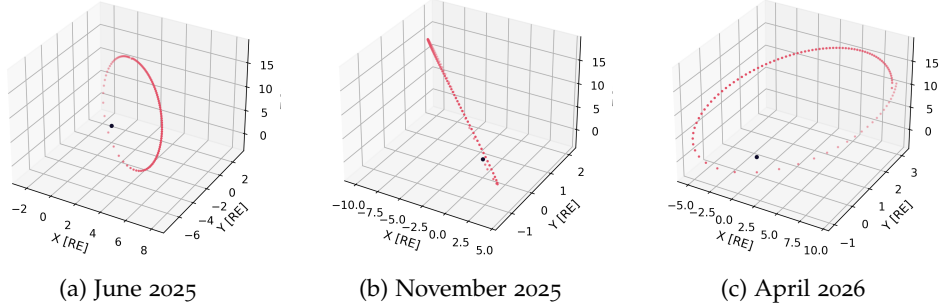
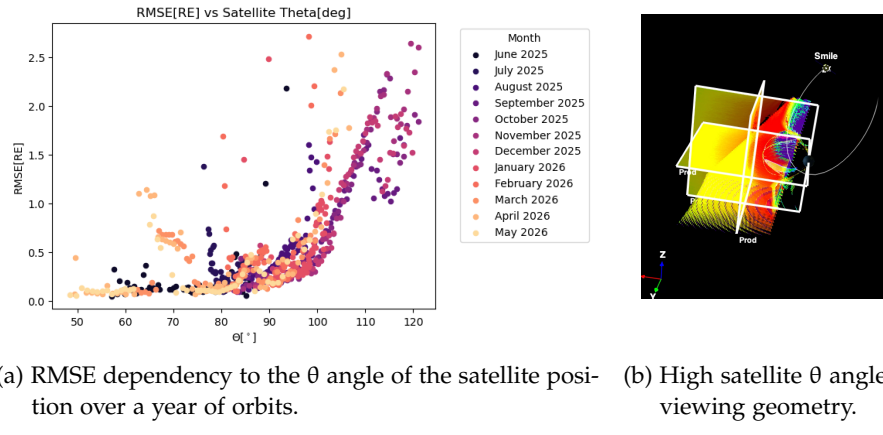


Figure 31: Orbit precession and corresponding viewing angles for June, November and April.

While, correlating the above orbits, as well the orbits for each month that are not explicitly discussed here, we see a clear dependency on the polar angle of the satellite’s position. In [Figure 32a](#) we notice that the error rapidly increases when the satellite is in the nightside, while there is no detection below  $50^\circ$  polar angle. The latter is to be expected, as we approach and enter the magnetopause for lower angles. We discussed previously the bias that the emission gradients could impose on the detection of the tangent direction. Here we see that for angles larger than  $90^\circ$  - when the satellite is in the nightside - this bias becomes rapidly important and the tangent hypothesis fails.



(a) RMSE dependency to the  $\theta$  angle of the satellite position over a year of orbits. (b) High satellite  $\theta$  angle viewing geometry.

Figure 32: Orbital dependency of RMSE over a year.

Looking into Figure 32, we see that this bias is not only attributed to the physical gradients, but also to the simulation restrictions. The simulation cube is restricted to  $z \in [-10, 10]$  RE, meaning that any emission outside this range is not captured in the integrated images. At the same time the magnetopause surface is constructed directly from the emission data of the simulation cube, meaning that the projected surface is limited in  $\theta \in [-65, 65]^\circ$ . For a full characterization of the high latitude angles, a simulation box to encapsulate all satellite positions and orbits will be necessary.

We pointed out earlier that we cannot extract meaningful information from the projection of the cusps in the image using the TFA. In other words, the use of a magnetopause model with strong cusp indentation does not represent the curve of the maximum intensity, that we want to fit. This opens the conversation on the definition of the magnetopause surface and the disagreement with the extracted surface, that we noticed in Section 2.1.4. When trying to fit empirical models, it was evident that their shape could not describe the discontinuous surface of the maximum intensity, nor the discontinuity predicted by the pressure equilibrium equation Equation 8.

Nguyen et al. re-enforces this disagreement by concluding that the Lin model overestimates the indentation of the cusps [11], when for the case of our extracted surface, every model severely underestimates it. In the last paper of his series, he explains the selection criteria for the crossings in the cusp region. He indicates the existence of two barriers - the inner and the outer cusp - and chooses the latter to perform the statistical analysis. This may be correlated with the second maximum emissivity of the 3D cube in that region, and further tests on the surface extraction shall be performed to understand how the empirical models correlate with the simulation results. Further metrics shall also be tested, emphasizing the dependency on the electromagnetic fields instead of the emission. The extraction of the magnetopause through the current sheet would be of particular interest, since its theoretical shape seems to better align with the empirical models. Future efforts shall concentrate on extracting the outer boundary, rejecting the inner cusp and defining coherently the magnetopause surface.

## TANGENT FITTING

---

In this chapter, we will develop a methodology to fit empirical models to the maximum intensity arc of the image, under the assumption that the tangent hypothesis holds true. As we saw in [Chapter 2](#), this depends strongly on the orbit and corresponding viewing angles of the satellite. We suppose here that this method will be utilized under the conditions dictated by the hypothesis and its limits. In this subset of cases, complete characterization of the method, shall also take into account the error propagation of the tangent hypothesis.

When trying to extract 3D information from a 2D image, we need to make some assumptions to account for the loss of information from the integration over the third axis. In the tangent fitting approach we attempt to reconstruct this information by assuming a particular shape for the magnetopause - an empirical model. A first approach could be, to trace the maximum intensity arc and then try to fit the model parameters to the arc, for that particular [POV](#). However, we already saw in [Section 2.2.2](#) that extracting a clean curve that follows the intended shape is not a simple extraction of the maximum intensity per row. Quite a few filters, as well as limits of steps were introduced to improve the detection, while the extraction still fails in certain viewing angles. We should also remember that the images that we are analyzing do not include any instrumental noise, background contributions or binning of the resolution. A more realistic image of what we expect the instrument to see, including background contribution, instrumental noise and resolution, is shown in [Figure 33](#). The [SXI](#) team has developed the relevant tools, not only to simulate the expected noise and background, but also to subtract it from the final images and aid in their processing.

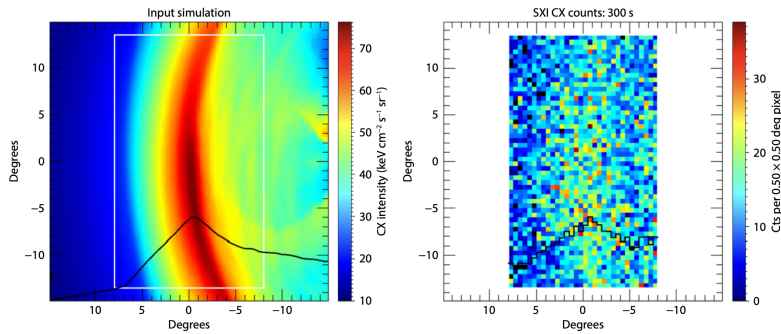


[Figure 33](#): Input image constructed from MHD simulations and output image of the SXI noise and background simulator. [[16](#)]

This is also the case for a [MHD](#) image, meaning that the details introduced by the test particles will make detection even more difficult. Therefore, a

different methodology was developed in order to address this problem and return the best fitted parameters of the empirical model simultaneously.

### 3.1 THE METHOD

The method that will be described in this section was inspired by a feature extraction technique used in image processing - the Hough Transform. The original Hough transform was developed to detect lines in an image, in order to support the detection of charged particles using bubble chambers [5]. Since then, it has been generalized to detect more shapes and has become a standard method in image processing and feature extraction.

The generalized Hough transform, normally needs an analytical function that can be discretized in order to transform from image to parameter space and vice-versa. As we will see below, deriving an analytical solution for the projection of complex 3D surfaces is not possible in most cases. Here, we develop a Hough-like voting method, by introducing a numerical approach to this projection problem.

We will demonstrate the methodology using the simplest empirical model, the Shue model. We generate a set of Shue surfaces for a range of the model's parameters,  $r_0$  and  $\alpha$ . To do this, we convert the Shue model to a 3D surface in spherical coordinates by rotating over the symmetry axis ( $x$ ) with the  $\phi$  angle. Due to its symmetrical nature, this results in the same expression:

$$r(\theta, \phi) = r_0 \left( \frac{2}{1 + \cos \theta} \right)^\alpha$$

*The Hough Transform is a feature extraction technique used in image analysis to find imperfect instances of shapes by a voting procedure in parameter space, from which object candidates are obtained as local maxima in a so-called accumulator space.*

For each of these surfaces we compute the tangent point to the satellite through a semi-analytical approach. We then convert to cartesian coordinates, thus parametrizing the surface with respect to  $\theta$  and  $\phi$ .

$$\begin{aligned} x &= r \cos \theta = r_0 \left( \frac{2}{1 + \cos \theta} \right)^\alpha \cos \theta \\ y &= r \sin \theta \cos \phi = r_0 \left( \frac{2}{1 + \cos \theta} \right)^\alpha \sin \theta \cos \phi \\ z &= r \sin \theta \sin \phi = r_0 \left( \frac{2}{1 + \cos \theta} \right)^\alpha \sin \theta \sin \phi \end{aligned}$$

Or in parametrized vector form:

$$\begin{aligned} R(\theta, \phi) &= \left( r_0 \left( \frac{2}{1 + \cos \theta} \right)^\alpha \cos \theta \right) \hat{i} + \left( r_0 \left( \frac{2}{1 + \cos \theta} \right)^\alpha \sin \theta \cos \phi \right) \hat{j} \\ &\quad + \left( r_0 \left( \frac{2}{1 + \cos \theta} \right)^\alpha \sin \theta \sin \phi \right) \hat{k} \end{aligned}$$

Having a parametrized surface, we can compute the normal vector function for each point, through the cross product of the partial derivative of this parametrized function, with respect to each parameter.

$$\begin{aligned} R_\theta &= \frac{\partial R}{\partial \theta} = r_0 \left( \frac{2}{1 + \cos \theta} \right)^\alpha \left[ \sin \theta \frac{(a - 1) \cos \theta - 1}{\cos \theta + 1} \hat{i} \right. \\ &\quad \left. + \cos \phi \left( \cos \theta + \frac{\sin^2 \theta a}{1 + \cos \theta} \right) \hat{j} \right. \\ &\quad \left. + \sin \phi \left( \cos \theta + \frac{\sin^2 \theta a}{1 + \cos \theta} \right) \hat{k} \right] \\ R_\phi &= \frac{\partial R}{\partial \phi} = r_0 \left( \frac{2}{1 + \cos \theta} \right)^\alpha \sin \theta (-\sin \phi \hat{j} + \cos \phi \hat{k}) \end{aligned}$$

Therefore, the normal vector function can be expressed as in [Equation 20](#)

$$\eta = R_\theta \times R_\phi = r_{\text{shue}}^2 \sin \theta \left[ \left( \cos \theta + \frac{\sin^2 \theta a}{1 + \cos \theta} \right) (\cos^2 \phi + \sin^2 \phi) \hat{i} \right] + \dots \hat{j} + \dots \hat{k} \quad (20)$$

We can now find the tangent direction in the FOV of the satellite by requesting that the normal vector and the vector that connects each point of the surface to the satellite, are perpendicular to each other. This gives us a set of  $(\theta, \phi)$  - a curve in 3D space. The tangent curve is given in GSE coordinates by [Equation 21](#), when solving for  $(x, y, z)$ .

$$\hat{\eta} \cdot \vec{r}_{\text{sat}} = 0 \implies (x_{\text{sat}} - x) r_0^2 \left( \frac{2}{1 + \cos \theta} \right)^{2\alpha} \sin \theta \left( \cos \theta + \frac{\sin^2 \theta a}{1 + \cos \theta} \right) + \dots = 0 \quad (21)$$

This is unsolvable analytically, or with series expansion, and therefore requires that we solve it numerically for each curve and each satellite [POV](#). It would be valuable to compare this with a fully numerical calculation of the normal vector function, as described in [Section 2.3.1](#), and optimize the projection process. In both cases the result is a set of points in the GSE frame. By applying a coordinate transformation from GSE to the [SXI](#) frame, as explained in [Section 2.3.1](#), we get a set of discretized curves, that correspond to the set of initial conditions of the Shue models. We interpolate the curves inside the FOV and rasterize them to the pixel grid of the image. A visualization of this process is shown in [Figure 34](#).

For each curve in the image coordinates, we calculate the intensity of the image along the curve and save its mean value in an array element. This gives us a measure of how prominent and bright this curve is in the image. We can now use this metric as a voting scheme between the curves by moving to the parameter space. Each curve and mean intensity correspond to specific initial parameters  $\alpha$  and  $r_0$ . We can construct a parameter matrix with the values of the mean intensity over each curve. The visualization of this matrix in a contour plot is shown in [Figure 35a](#). In this figure, the maximum value in parameter space is noted with the red dot. The coordinates of this point, correspond to the model parameters that return the brightest projection in the image. Moving back to image space, we plot only the curve that correspond to these parameters in [Figure 35b](#), denoted with the blue line.

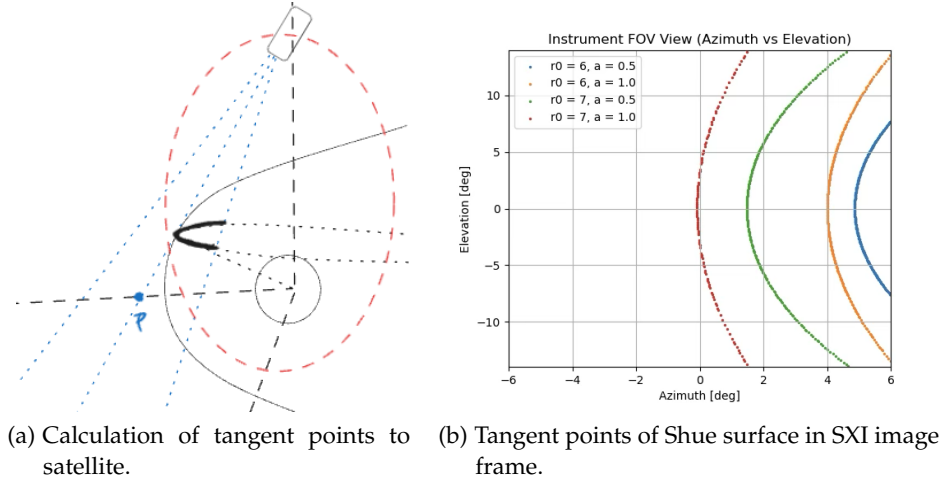


Figure 34: Projecting the tangent points of Shue surfaces.

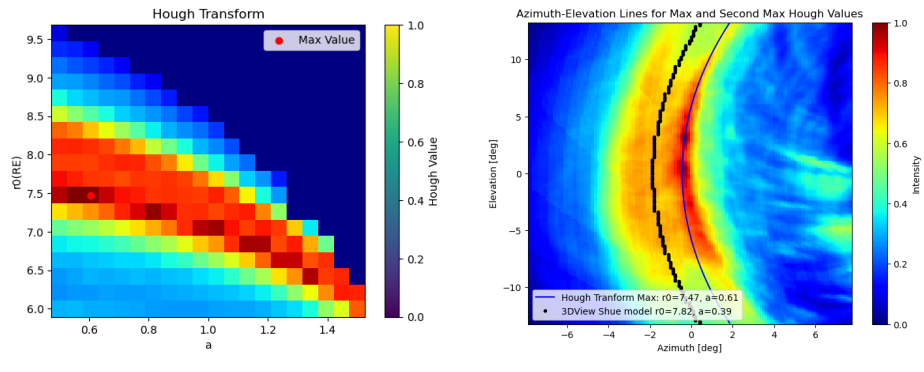


Figure 35: Parameter and Image space of Hough transform.

### 3.2 BENCHMARKING THE FITTING METHOD

A measure of the error of this method is necessary, both for the characterization of the method itself, but also for an in-orbit metric of its accuracy. We will attempt the first through comparison with the simulation and the latter through the image data alone.

#### 3.2.1 Image-fitted Shue to cube-fitted Shue

We can characterize the method by benchmarking it to the expected position of the magnetopause according to the simulation cube. As we saw in [Section 2.1](#), extracting the true magnetopause from the cube is not as simple as it appears, the main obstacles being the inhomogeneous behavior of the test particles, but more importantly the ambiguity of defining such a surface consistently. We can, however, run a simple test by comparing the fitted Shue

surface to the Shue surface that can best describe the 3D simulation data - a model fitted directly to the cube. For simplicity, we will use the parameters that were fitted in [Section 2.1.2](#) -  $r_0 = 7.82 \text{ RE}$  and  $\alpha = 0.386$ .

Running the Hough method for a full orbit, we can get the evolution of the estimated parameters, as well as their error compared to the initial model. We remind the reader that the simulation is a steady state instance and therefore the variability of the detected parameters is attributed solely to the viewing angle. [Figure 36](#) shows the evolution of the estimated subsolar distance  $r_0$  with time, for a full summer orbit of August 2025.

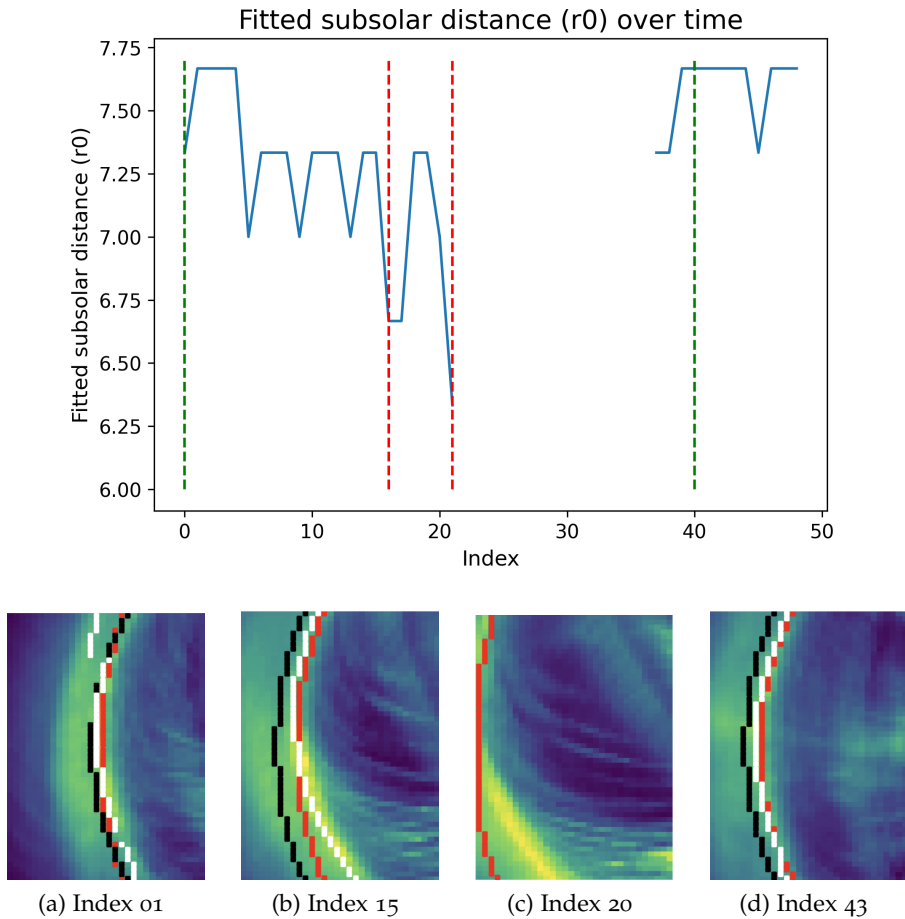


[Figure 36](#): Evolution of  $r_0$  over time elapsed from 1st August 2025 09:00 UTC and key snapshots. Snapshots 15 and 20 are denoted with the red dotted line, and snapshots 01 and 43 with the green. The black line is the projection of the cube-fitted model, the red line the image-fitted model, and the white the maximum intensity arc.

In [Figure 36](#) strong variation is observed depending on the position of the satellite. The clipping of the  $r_0$  values is the result of the discretization of the parameter space in a grid. The green dotted lines, indicating low error detection, are correlated with [POVs](#) where the image arc appears symmetrical. The indentation of the cusps is responsible for this seeming asymmetry we observe in the snapshots of the red dotted lines of [Figure 36](#). This is to be expected since the Shue model is symmetrical and does not describe any in-

dentation, and therefore cannot capture these shapes. This is reflected in the evolution of the error shown in [Figure 37](#), where in this orbit the satellite sees increasingly the cusp as it approaches the magnetopause. A visualization of the images throughout the orbit is provided in the appendix, [Figure 43](#).

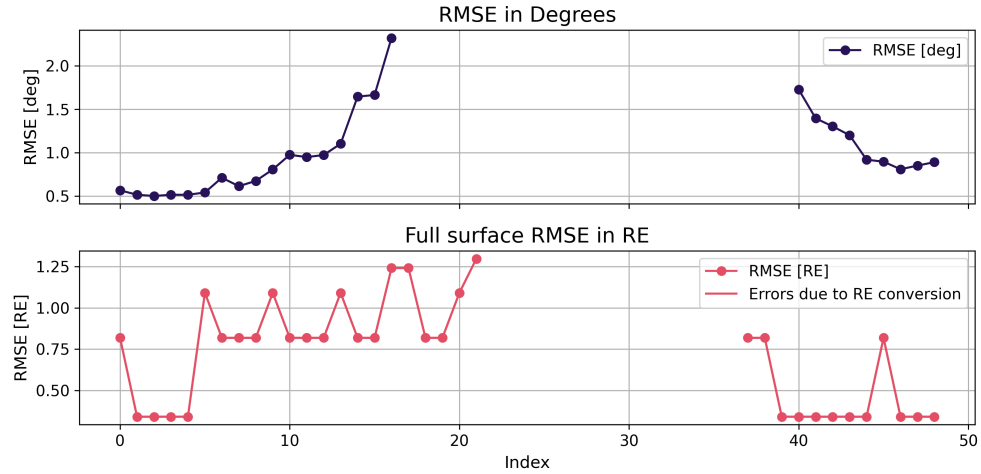


Figure 37: Cube-fitted Shue model to Image-fitted model RMSE in degrees and RE.

Since, we are mainly interested in the subsolar distance estimation, it is useful to plot the deviation of  $r_0$  from the initial parameter, as in [Figure 38](#). We notice that for the symmetric cases, we get error close to 0.5 RE which is the [SXI](#) requirement. This has a non-negligible contribution from the discretization of the parameter space and can be improved through the deployment of fitting schemes as will be discussed in [Section 3.2.3](#). Evidently, another important contribution in this error is the simplicity of the model itself, and can be improved by using more sophisticated models such as the Lin or the Liu model. However, these first test shows that although we used a sparsely sampled parameter space and a simplistic model, we can still get information about the subsolar distance with an error close to the requirement. We therefore expect the improvements suggested here to lead to increased accuracy.

Contrary to the subsolar distance, the flaring parameter is more challenging to be determined through this method. This is logical, since the asymmetry of the image arc would be interpreted as increased or decreased flaring in a symmetric model. To understand the capabilities of this method in regard to other parameters, we shall run this tests using more descriptive empirical models.

### 3.2.2 Characterization through maximum intensity curve

Although we expect the simulation to be representative of the magnetopause to some extent, we also expect to be surprised. Having a metric to characterize our measurement without a simulation dependency is crucial for the analysis of the real data. We can achieve this by benchmarking the fitted

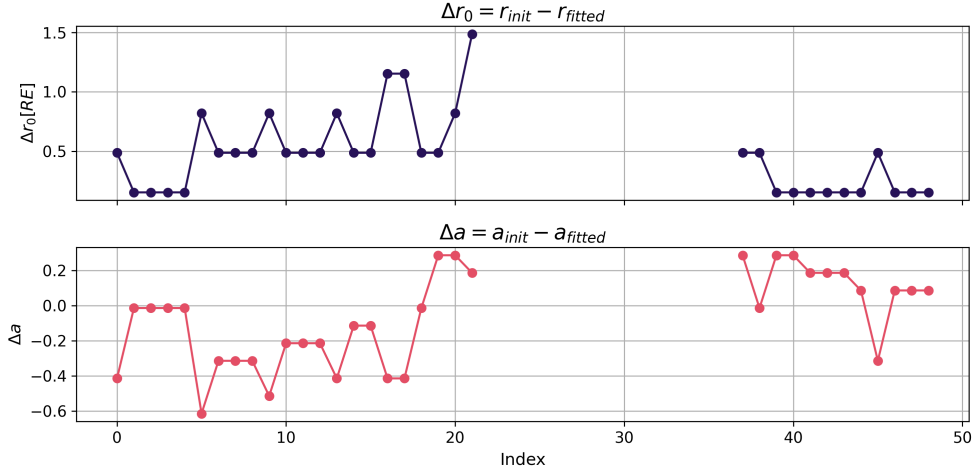


Figure 38: Deviation of image-fitted parameters from initial cube-fitted parameters  $r_0$  and  $\alpha$ .

curve to the maximum intensity arc of the image. Thus, we can have a metric of the error of the fit, but also of the agreement of the empirical model to the true shape of the magnetopause.

The latter is particularly important, since it is challenging to derive the global shape of the magnetopause from in-situ measurements alone - meaning that there is still disagreement on its shape and its response to the solar wind. Using a non-representative empirical surface would automatically result in different projected curve geometries, that could not capture the maximum arc shape, no matter the fitting process. The error therefore, between the fitted models through the Hough method and the maximum intensity arc can be used as a metric to characterize the empirical model themselves.

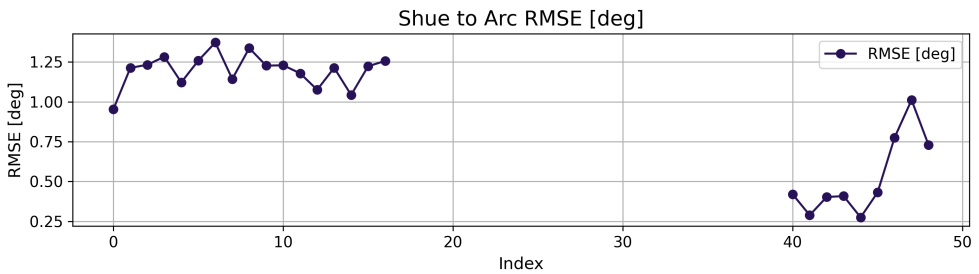


Figure 39: Evolution of fitted Shue curves to maximum intensity arcs RMSE over time elapsed from 1st August 2025 09:00 UTC.

The evolution of this metric for the August orbit is shown in Figure 39. Here we have contribution both from the arc extraction problems that we were facing in Section 2.2.2, and from the fitting errors we analyzed above. Better image processing is crucial for this metric to return a reliable estimation of the empirical model error alone. This can be seen in the first snapshot of Figure 36, where there seems to be a good fit of the model, but the maximum intensity arc extraction fails. However, cases like the symmetric

view of [Figure 36d](#) combined with the extraction of the intended arc, return promising results.

### 3.2.3 Discussion and Future developments

In this chapter we presented the methodology that was developed to fit empirical magnetopause models to the structured integrated images of the [LaTeP](#) model. We also characterized its accuracy for a full summer orbit, using two proposed metrics: the simulation to image projection [RMSE](#) and the maximum intensity arc to image projection [RMSE](#). We performed this analysis using the Shue magnetopause model for simplicity.

Full characterization of the method would require the correlation of these results with the orbital elements of the satellite, since the orbit is not finalized. To do this we shall run full year orbits as we did in [Section 2.3.2](#) and correlate the RMSE with the satellite position and the seasonality. Under the scope of facilitating the analysis of multiple orbits, the fitting scheme, as well as the projection of the surfaces shall be optimized.

The smooth behavior of the parameter space allows for the deployment of methods such as stochastic descend (ascend in our case) to find the global maximum, without the need to calculate each projection of the parameter space. A plethora of fitting schemes can be utilized, due to this continuous behavior, and we shall not restrict ourselves to the one mentioned above. The projection itself is relatively costly in terms of computational time, since it is being performed as many times as the resolution of the parameter grid. We shall therefore look into comparing the numerical with the semi-analytical approach, as well as building a 3D numerical solver instead of simply using a mask to find the tangent points. Finally, as of now, we compute the full tangent curve and then limit it to the [FOV](#). It would be useful to try building the grid of the magnetopause only in the space inside the [FOV](#), although this may prove to be complicated using spherical coordinates. A solution could be to build a grid directly from the FOV cone of the instrument, however this would result in a 3D grid, when currently the spherical grid needs only two parameters since  $r$  is a function of  $\theta$  and  $\phi$ .

Having optimized the code, further tests shall be performed to derive the accumulated error from the tangent hypothesis and the fitting process. Such tests could be benchmarking the fitted curve to the magnetopause extracted from the simulation cube. More sophisticated models that can capture the cusp indentation, as well as asymmetries, shall also be implemented to test the limits of the parameters that can be fitted using information from a single image. Finally, full characterization of the method can be performed by having a representative surface - not only for the benchmarking but for the fitting itself. In this light, parametrizing the simulation magnetopause surface and using it to fit the maximum intensity arcs, would allow for a complete characterization of the method in its static case. Of course, this implicates the definition problems that we faced in [Section 2.3.2](#) and the limits of each detection method should be taken into account.

We have shown that depending on the geometry, the method can be utilized to derive useful information about the magnetopause and its response to the solar wind. Depending on the performance of other techniques, it can be also utilized to provide initial parameters to [BFA](#) methods that require good initial parameter estimation. In contrary to these techniques however, it has no dependency to the simulation itself, and can therefore independently characterize existing empirical models. A combination of such methods will result to the maximum scientific output. Further work on the characterization of these methods will be essential to determine the optimal operations and science plan for the [SMILE](#) mission.

a

## PERFORMANCE OVER MULTIPLE ORBITS

### A.1 TANGENT HYPOTHESIS

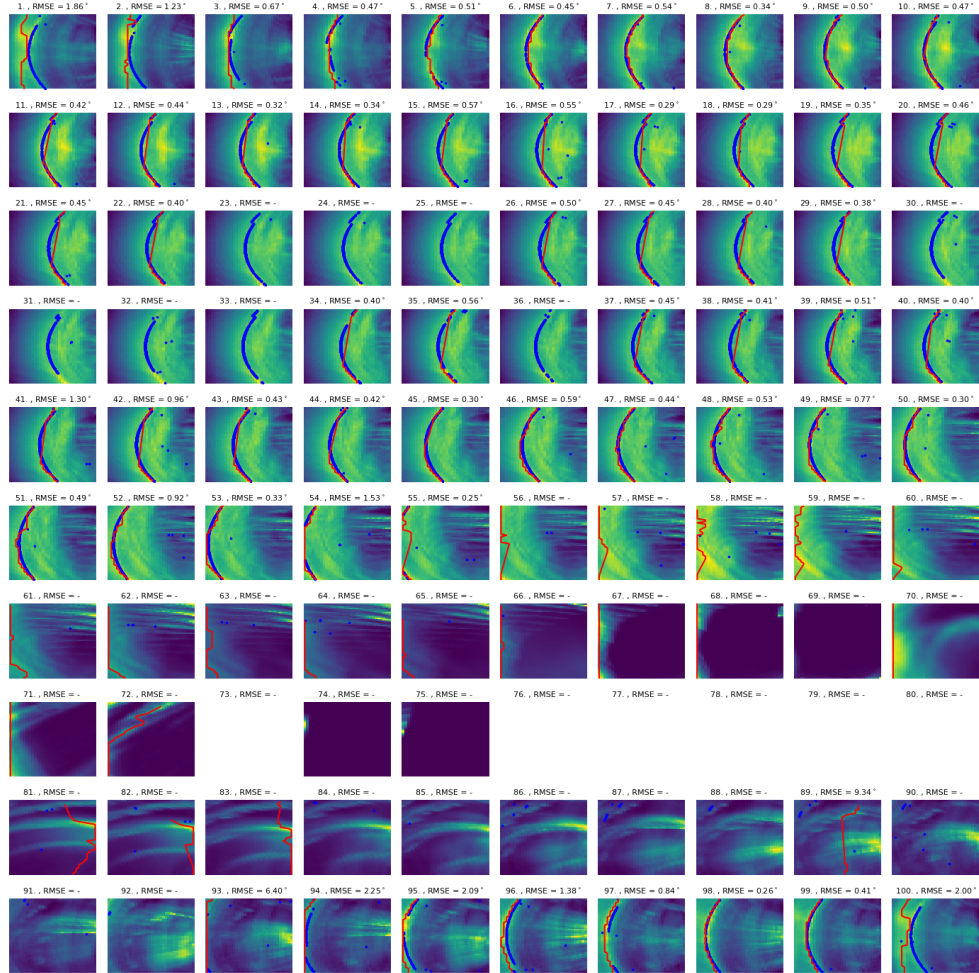


Figure 40: Full orbit images for June 2025. The red line denotes the maximum intensity arc, and the blue line the surface projection.

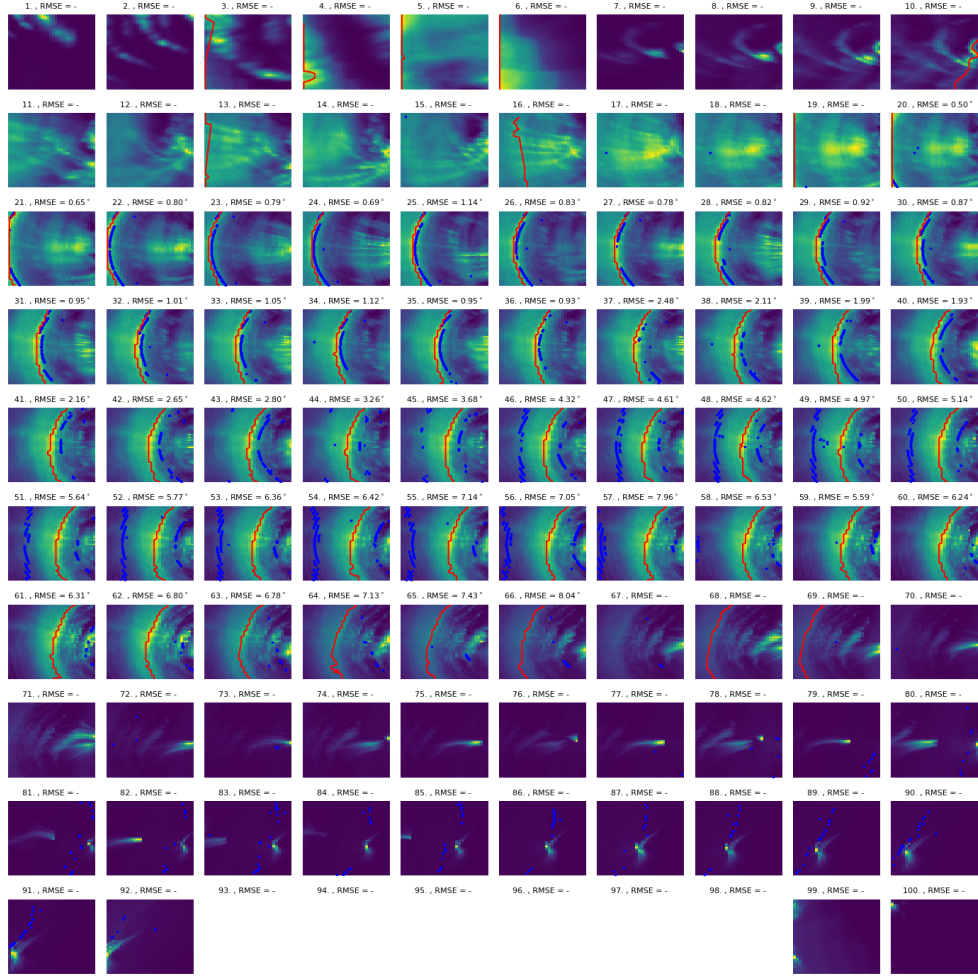


Figure 41: Full orbit images for November 2025. The red line denotes the maximum intensity arc, and the blue line the surface projection.

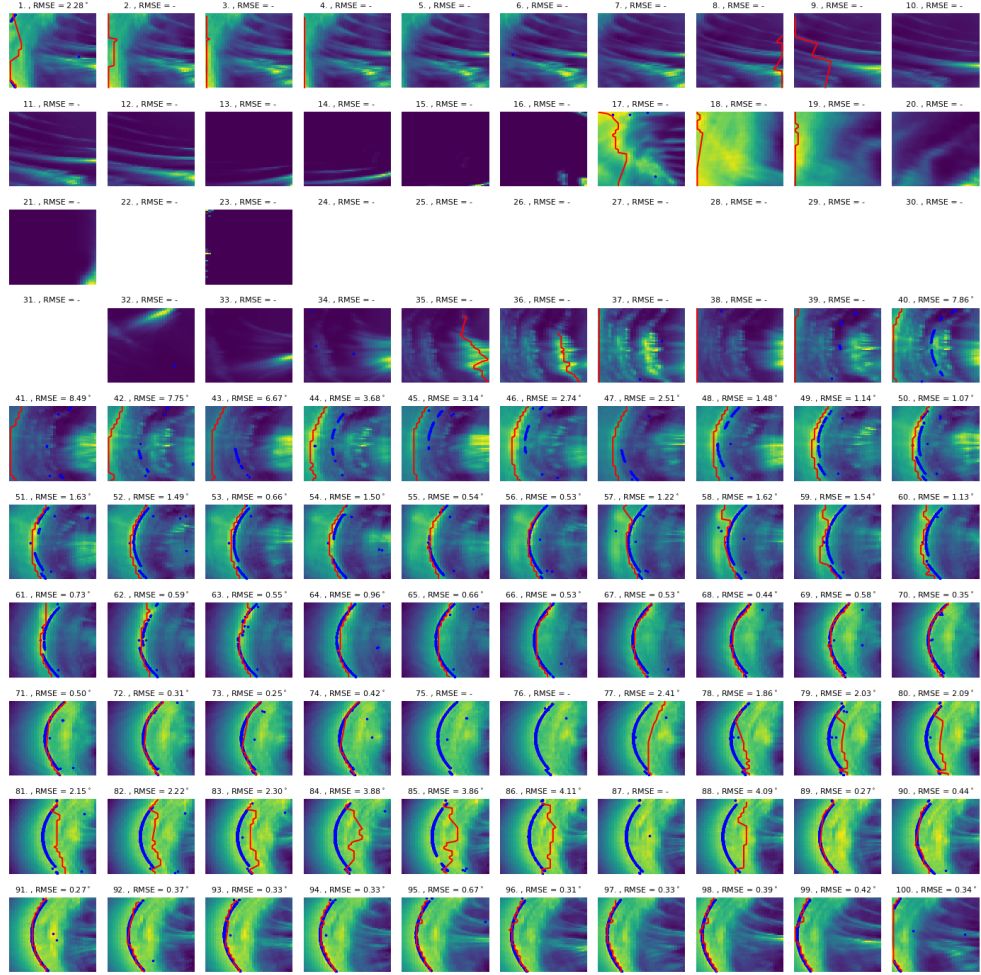


Figure 42: Full orbit images for April 2026. The red line denotes the maximum intensity arc, and the blue line the surface projection.

## A.2 TANGENT FITTING

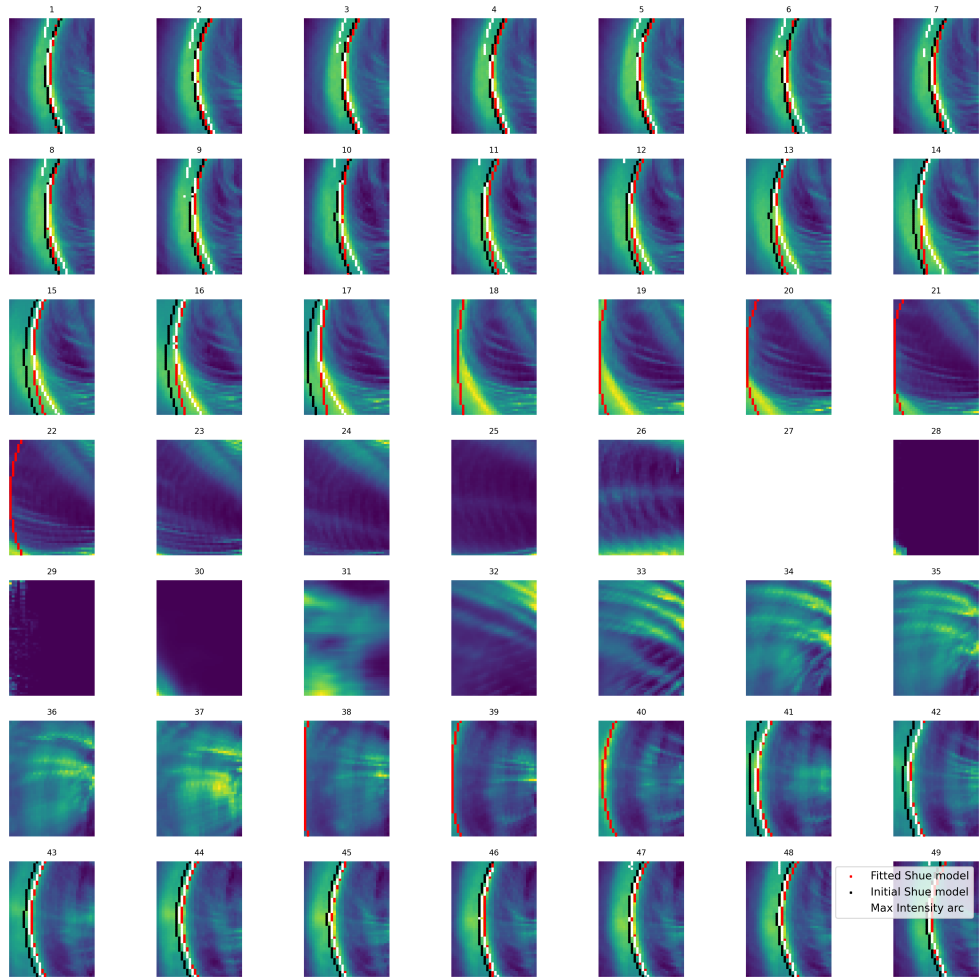


Figure 43: Full orbit images for August 2025. The white line denotes the maximum intensity arc, the red line the fitted Shue model, and the blue line the surface projection.

## BIBLIOGRAPHY

---

- [1] Wolfgang Baumjohann and Rudolf A. Treumann. *Basic space plasma physics*. Reprinted. London: Imperial College Press, 2006. 329 pp. ISBN: 978-1-86094-079-8.
- [2] Michael R. Collier and Hyunju K. Connor. "Magnetopause Surface Reconstruction From Tangent Vector Observations." In: *Journal of Geophysical Research: Space Physics* 123.12 (Dec. 2018). ISSN: 2169-9380, 2169-9402. DOI: [10.1029/2018JA025763](https://doi.org/10.1029/2018JA025763). URL: <https://agupubs.onlinelibrary.wiley.com/doi/10.1029/2018JA025763> (visited on 06/11/2025).
- [3] T. E. Cravens. "Comet Hyakutake x-ray source: Charge transfer of solar wind heavy ions." In: *Geophysical Research Letters* 24.1 (1997), pp. 105–108. DOI: <https://doi.org/10.1029/96GL03780>.
- [4] V. Génot et al. "Science data visualization in planetary and heliospheric contexts with 3DView." In: *Planetary and Space Science* 150 (2018). Enabling Open and Interoperable Access to Planetary Science and Helio-physics Databases and Tools, pp. 111–130. ISSN: 0032-0633. DOI: <https://doi.org/10.1016/j.pss.2017.07.007>. URL: <https://www.sciencedirect.com/science/article/pii/S003206331630383X>.
- [5] P. V. C. Hough. *METHOD AND MEANS FOR RECOGNIZING COMPLEX PATTERNS*. US Patent 3,069,654. Dec. 1962. URL: <https://www.osti.gov/biblio/4746348>.
- [6] Anders M. Jorgensen, Tianran Sun, Chi Wang, Lei Dai, Steven Sem-bay, Fei Wei, Yihong Guo, and Ronglan Xu. "Boundary Detection in Three Dimensions With Application to the SMILE Mission: The Effect of Photon Noise." In: *Journal of Geophysical Research: Space Physics* 124.6 (June 2019), pp. 4365–4383. ISSN: 2169-9380, 2169-9402. DOI: [10.1029/2018JA025919](https://doi.org/10.1029/2018JA025919). URL: <https://agupubs.onlinelibrary.wiley.com/doi/10.1029/2018JA025919> (visited on 06/11/2025).
- [7] R. L. Lin, X. X. Zhang, S. Q. Liu, Y. L. Wang, and J. C. Gong. "A three-dimensional asymmetric magnetopause model." In: *Journal of Geophysical Research: Space Physics* 115.A4 (2010). DOI: <https://doi.org/10.1029/2009JA014235>. eprint: <https://agupubs.onlinelibrary.wiley.com/doi/pdf/10.1029/2009JA014235>. URL: <https://agupubs.onlinelibrary.wiley.com/doi/abs/10.1029/2009JA014235>.
- [8] C. M. Lisse et al. "Discovery of X-ray and Extreme Ultraviolet Emission from Comet C/Hyakutake 1996 B2." In: *Science* 274.5285 (1996), pp. 205–209. DOI: [10.1126/science.274.5285.205](https://doi.org/10.1126/science.274.5285.205). eprint: <https://www.science.org/doi/pdf/10.1126/science.274.5285.205>. URL: <https://www.science.org/doi/abs/10.1126/science.274.5285.205>.

- [9] Z.-Q. Liu, J. Y. Lu, C. Wang, K. Kabin, J. S. Zhao, M. Wang, J. P. Han, J. Y. Wang, and M. X. Zhao. "A three-dimensional high Mach number asymmetric magnetopause model from global MHD simulation." In: *Journal of Geophysical Research: Space Physics* 120.7 (2015), pp. 5645–5666. DOI: <https://doi.org/10.1002/2014JA020961>. eprint: <https://agupubs.onlinelibrary.wiley.com/doi/pdf/10.1002/2014JA020961>. URL: <https://agupubs.onlinelibrary.wiley.com/doi/abs/10.1002/2014JA020961>.
- [10] G. Nguyen, N. Aunai, B. Michotte De Welle, A. Jeandet, B. Lavraud, and D. Fontaine. "Massive Multi-Mission Statistical Study and Analytical Modeling of the Earth's Magnetopause: 1. A Gradient Boosting Based Automatic Detection of Near-Earth Regions." In: *Journal of Geophysical Research: Space Physics* 127.1 (). DOI: [10.1029/2021ja029773](https://doi.org/10.1029/2021ja029773).
- [11] G. Nguyen, N. Aunai, B. Michotte De Welle, A. Jeandet, B. Lavraud, and D. Fontaine. "Massive Multi-Mission Statistical Study and Analytical Modeling of the Earth's Magnetopause: 4. On the Near-Cusp Magnetopause Indentation." In: *Journal of Geophysical Research: Space Physics* 127 (). DOI: [10.1029/2021ja029776](https://doi.org/10.1029/2021ja029776).
- [12] E. N. Parker. "Dynamics of the Interplanetary Gas and Magnetic Fields." In: *The Astrophysical Journal* 128 (Nov. 1958), p. 664. ISSN: 0004-637X, 1538-4357. DOI: [10.1086/146579](https://doi.org/10.1086/146579). URL: <http://adsabs.harvard.edu/doi/10.1086/146579> (visited on 06/09/2025).
- [13] Andrew Read. "On the apparent line-of-sight alignment of the peak X-ray intensity of the magnetosheath and the tangent to the magnetopause, as viewed by SMILE-SXI." In: *Earth and Planetary Physics* 8.1 (), pp. 155–172. DOI: [10.26464/epp2023062](https://doi.org/10.26464/epp2023062).
- [14] I. P. Robertson and T. E. Cravens. "X-ray emission from the terrestrial magnetosheath." In: *Geophysical Research Letters* 30.8 (2003). DOI: <https://doi.org/10.1029/2002GL016740>.
- [15] Andrey Samsonov, Steven Sembay, Andrew Read, Jennifer Alyson Carter, Graziella Branduardi-Raymont, David Sibeck, and Philippe Escoubet. "Finding Magnetopause Standoff Distance Using a Soft X-ray Imager: 2. Methods to Analyze 2-D X-ray Images." In: *Journal of Geophysical Research: Space Physics* 127.12 (2022). DOI: <https://doi.org/10.1029/2022JA030850>.
- [16] S. Sembay et al. "The Soft X-ray Imager (SXI) on the SMILE Mission." In: *Earth and Planetary Physics* 8.1 (), pp. 5–14. DOI: [10.26464/epp2023067](https://doi.org/10.26464/epp2023067).
- [17] J.-H. Shue, J. K. Chao, H. C. Fu, C. T. Russell, P. Song, K. K. Khurana, and H. J. Singer. "A new functional form to study the solar wind control of the magnetopause size and shape." In: *Journal of Geophysical Research: Space Physics* 102.A5 (1997), pp. 9497–9511. DOI: <https://doi.org/10.1029/97JA00196>. eprint: <https://agupubs.onlinelibrary.wiley.com/doi/pdf/10.1029/97JA00196>.

- wiley.com/doi/pdf/10.1029/97JA00196. URL: <https://agupubs.onlinelibrary.wiley.com/doi/abs/10.1029/97JA00196>.
- [18] David Sibeck et al. “Imaging Plasma Density Structures in the Soft X-Rays Generated by Solar Wind Charge Exchange with Neutrals.” In: *Space Science Reviews* 214 (June 2018). doi: [10.1007/s11214-018-0504-7](https://doi.org/10.1007/s11214-018-0504-7).
  - [19] Tianran Sun, Chi Wang, Hyunju K. Connor, Anders M. Jorgensen, and Steven Sembay. “Deriving the Magnetopause Position from the Soft X-Ray Image by Using the Tangent Fitting Approach.” In: *Journal of Geophysical Research: Space Physics* 125.9 (), e2020JA028169. doi: [10.1029/2020JA028169](https://doi.org/10.1029/2020JA028169).
  - [20] S. J. Wharton, J. A. Carter, S. Sembay, Y. Soobiah, S. Nitti, and T. R. Sun. “Modeling the Magnetospheric 3D X-Ray Emission From SWCX Using a Cusp-Magnetosheath Emissivity Model.” In: *Journal of Geophysical Research: Space Physics* 130.2 (Feb. 2025), e2024JA033307. ISSN: 2169-9380, 2169-9402. doi: [10.1029/2024JA033307](https://doi.org/10.1029/2024JA033307). URL: <https://agupubs.onlinelibrary.wiley.com/doi/10.1029/2024JA033307> (visited on 06/07/2025).
  - [21] Qiuyu Xu, Dimitra Koutroumpa, Ronan Modolo, Tianran Sun, Hyunju Connor, Steve Sembay, and Yevhen Tkachenko. “Modeling Soft X-Ray Emissions at the Dayside Magnetopause.” In: *Journal of Geophysical Research: Space Physics* 129.8 (Aug. 2024), e2024JA032687. ISSN: 2169-9380, 2169-9402. doi: [10.1029/2024JA032687](https://doi.org/10.1029/2024JA032687). URL: <https://agupubs.onlinelibrary.wiley.com/doi/10.1029/2024JA032687> (visited on 06/11/2025).